Research Square

Preprints are preliminary reports that have not undergone peer review.
They should not be considered conclusive, used to inform clinical practice,
or referenced by the media as validated information.

Integrative analysis of cell death- and senescence-associated transcriptional programs identifies molecular subtypes and key genes in clear cell renal cell carcinoma

Xiangyi Wang
Nanchang University
Hao Hu
Nanchuan Hospital of Chongqing Medical University
Kaihong Wang
ndyfy05955@ncu.edu.cn

Nanchang University

Research Article

Keywords: clear cell renal cell carcinoma, regulated cell death, cellular senescence, integrative genomics, tumor immune microenvironment, network perturbation

Posted Date: November 18th, 2026

DOI: https://doi.org/10.21203/rs.3.rs-11446663/v1

License: This work is licensed under a Creative Commons Attribution 4.0 International License.
Read Full License

Additional Declarations: No competing interests reported.

Integrative analysis of cell death- and senescence-associated transcriptional programs identifies molecular subtypes and key genes in clear cell renal cell carcinoma

Xiangyi Wang[1], Hao Hu[2], Kaihong Wang[1]*

[1]Department of Urology, The First Affiliated Hospital, Jiangxi Medical College, Nanchang University, Nanchang 330000, China.

[2]Department of Urology, Nanchuan Hospital of Chongqing Medical University, No. 16, South Street, Nanchuan District 408400, Chongqing,China

*** Correspondence:**

Corresponding Author:Kaihong Wang

ndyfy05955@ncu.edu.cn

Abstract

Clear cell renal cell carcinoma (ccRCC) exhibits substantial molecular and immune heterogeneity, yet the role of integrated cell death- and senescence-associated (CDS) programs remains incompletely understood. We characterized 21 CDS transcriptional signatures using multicohort transcriptomic, clinical, pharmacogenomic, and single-cell data. Consensus clustering of 538 TCGA-KIRC tumors identified three subtypes characterized by metabolic–proliferative, immune–inflammatory, and hypoxia–angiogenesis-associated profiles. The immune-enriched C2 subtype showed the poorest survival with elevated exhausted and regulatory T-cell signatures. Focusing on C2, edge perturbation analysis identified 246 network-associated genes, which were narrowed to 23 CDS-related candidates and 12 survival-associated genes. Among 101 machine-learning combinations, CoxBoost followed by random survival forest achieved the best performance, generating a ten-gene prognostic signature with a mean C-index of 0.733 across five cohorts. The resulting risk score was associated with survival outcomes and adverse clinicopathological characteristics. Among the ten genes,

LMNB1, LY96, and HSPA8 were further investigated based on their differential expression and high tumor–normal discrimination AUCs. Single-cell profiling and virtual knockout analyses linked LMNB1 to T-cell cytotoxicity-associated networks, LY96 to macrophage antigen-presentation programs, and HSPA8 to T-cell cytokine signaling. Pharmacogenomic analysis identified nine compounds with differential predicted drug responses in C2. Across three independent treatment cohorts, C2 consistently exhibited the lowest response rates. Collectively, these findings demonstrate that integrated CDS transcriptional profiling delineates prognostically distinct molecular states in ccRCC, revealing an immune-enriched yet unfavorable subtype and identifying candidate genes that link cellular stress-associated programs to tumor immune heterogeneity.

Keywords: clear cell renal cell carcinoma; regulated cell death; cellular senescence; integrative genomics; tumor immune microenvironment; network perturbation

Introduction

Clear cell renal cell carcinoma (ccRCC) is the most common histological subtype of renal cell carcinoma, accounting for approximately 75–80% of cases. Although localized disease can often be managed surgically, clinical outcomes in advanced ccRCC remain heterogeneous despite advances in immune checkpoint blockade and antiangiogenic therapies[1,2]. Genomic and molecular studies have identified VHL inactivation, hypoxia-inducible factor signaling, chromatin-remodeling alterations, metabolic reprogramming, and extensive intratumoral heterogeneity as defining features of ccRCC[3–5]. Together with its complex immune microenvironment, these characteristics highlight the importance of understanding how cellular stress-response programs relate to molecular heterogeneity and clinical outcomes[6,7].

Regulated cell death and cellular senescence represent distinct yet interconnected responses to cellular stress. Multiple regulated cell death pathways influence tissue homeostasis, inflammation, and antitumor immunity, while cellular senescence is characterized by sustained cell-cycle arrest and context-dependent secretory responses[8–10]. Although senescence can suppress malignant transformation, persistent senescence-associated programs may contribute to chronic inflammation, tissue remodeling, and tumor progression[11,12]. Notably,

experimental VHL inactivation can induce an Rb-dependent, hypoxia-inducible-factor-independent senescence response [13], providing a biological rationale for jointly investigating cell death- and senescence-associated (CDS) transcriptional programs in ccRCC.

Previous studies have linked individual regulated cell death pathways, including immunogenic cell death, to prognosis and immune microenvironment characteristics in ccRCC[14,15]. More recently, integrated profiling of 21 CDS signatures revealed distinct molecular subtypes and immune microenvironment features in lung adenocarcinoma[16]. However, the combined transcriptional organization of cell death and senescence programs in ccRCC, particularly its associations with immune heterogeneity and clinical outcomes, remains incompletely characterized. Furthermore, integrating CDS transcriptional profiles with molecular interaction networks may help identify candidate genes associated with distinct tumor states and provide insights into their potential cellular functions.

Here, we systematically characterized 21 CDS signatures across TCGA-KIRC and additional ccRCC cohorts to investigate molecular heterogeneity, immune microenvironment features, and treatment-related associations. Focusing on the subtype associated with unfavorable survival, we integrated sample-specific edge perturbation analysis with multicohort machine learning to identify CDS-related candidate genes and establish a prognostic signature. We further characterized selected genes through multicohort expression and clinical analyses, followed by single-cell transcriptomic profiling and computational virtual knockout analysis to explore their cellular distributions and potential functional associations. This integrative approach provides a framework for understanding the relationships among CDS-associated transcriptional programs, molecular heterogeneity, immune regulation, and prognosis in ccRCC.

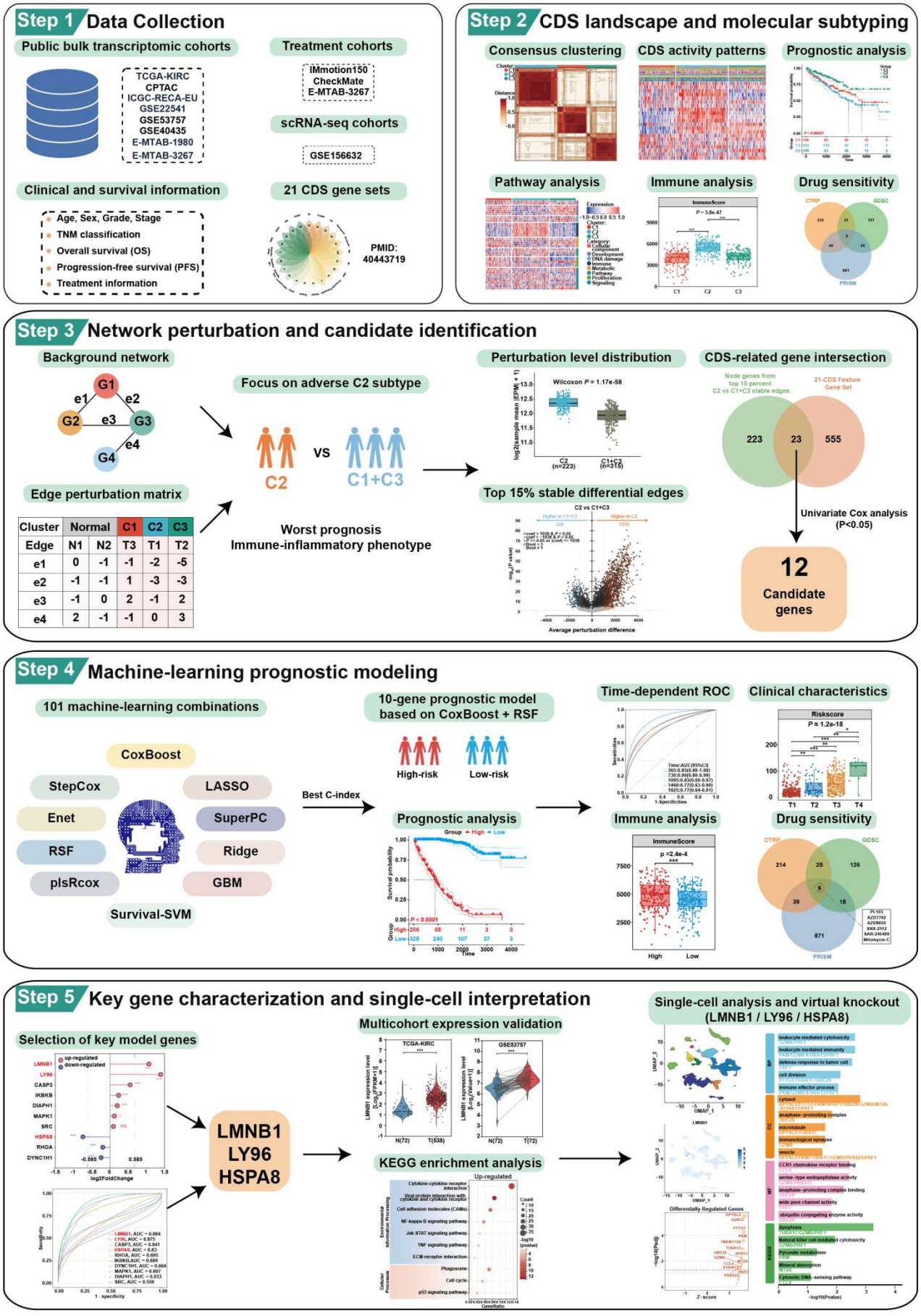

Step 1 Data Collection
Public bulk transcriptomic cohorts
TCGA-KIRC
CPTAC
ICGC-RECA-EU
GSE22541
GSE53757
GSE40435
E-MTAB-1980
E-MTAB-3267
Treatment cohorts
IMmotion150
CheckMate
E-MTAB-3267
scRNA-seq cohorts
GSE156632
Clinical and survival information
Age, Sex, Grade, Stage
TNM classification
Overall survival (OS)
Progression-free survival (PFS)
Treatment information
21 CDS gene sets
PMID: 40443719
Step 2 CDS landscape and molecular subtyping
Consensus clustering
CDS activity patterns
Prognostic analysis
Pathway analysis
Immune analysis
Drug sensitivity
Step 3 Network perturbation and candidate identification
Background network
G1
G2
G3
G4
e1
e2
e3
e4
Edge perturbation matrix
Cluster | Normal | | C1 | C2 | C3
Edge | N1 | N2 | T3 | T1 | T2
e1 | 0 | -1 | -1 | -2 | -5
e2 | -1 | -1 | 1 | -3 | -3
e3 | -1 | 0 | 2 | -1 | 2
e4 | 2 | -1 | -1 | 0 | 3
Focus on adverse C2 subtype
C2
vs
C1+C3
Worst prognosis
Immune-inflammatory phenotype
Perturbation level distribution
Wilcoxon P = 1.17e-58
log2(sample mean (EPM(+ 1)
C2 (n=223)
C1+C3 (n=315)
Top 15% stable differential edges
C2 vs C1+C3
Higher in C1+C3
Higher in C2
Average perturbation difference
CDS-related gene intersection
Node genes from top 15 percent C2 vs C1+C3 stable edges
21-CDS Feature Gene Set
223
23
555
Univariate Cox analysis (P<0.05)
12
Candidate genes
Step 4 Machine-learning prognostic modeling
101 machine-learning combinations
CoxBoost
StepCox
LASSO
Enet
SuperPC
RSF
Ridge
plsRcox
GBM
Survival-SVM
Best C-index
10-gene prognostic model based on CoxBoost + RSF
High-risk
Low-risk
Prognostic analysis
Group High Low
Survival probability
P < 0.0001
Time
Time-dependent ROC
Sensitivity
1-Specificities
Immune analysis
ImmuneScore
p =2.4e-4
High
Low
Clinical characteristics
Riskscore
P = 1.2e-18
T1
T2
T3
T4
Drug sensitivity
CTRP
GDSC
PRISM
Step 5 Key gene characterization and single-cell interpretation
Selection of key model genes
LMNB1
LY96
CASP3
IKBKB
DIAPH1
MAPK1
SRC
HSPA8
RHOA
DYNC1H1
up-regulated
down-regulated
log2FoldChange
Sensitivity
1 - specificity
LMNB1, AUC = 0.884
LY96, AUC = 0.875
CASP3, AUC = 0.841
HSPA8, AUC = 0.83
RHOA, AUC = 0.695
IKBKB, AUC = 0.689
DYNC1H1, AUC = 0.664
MAPK1, AUC = 0.637
DIAPH1, AUC = 0.633
SRC, AUC = 0.559
LMNB1
LY96
HSPA8
Multicohort expression validation
TCGA-KIRC
GSE53757
LMNB1 expression level [Log2(FPKM+1)]
LMNB1 expression level [Log2(Value+1)]
N(72)
T(538)
T(72)
KEGG enrichment analysis
Up-regulated
Cytokine-cytokine receptor interaction
Viral protein interaction with cytokine and cytokine receptor
Cell adhesion molecules (CAMs)
NF-kappa B signaling pathway
Jak-STAT signaling pathway
TNF signaling pathway
ECM-receptor interaction
Phagosome
Cell cycle
p53 signaling pathway
Environmental Information Processing
Cellular Processes
Count
-log10 (pvalue)
GeneRatio
Single-cell analysis and virtual knockout (LMNB1 / LY96 / HSPA8)
UMAP_1
UMAP_2
LMNB1
Differentially Regulated Genes
Z-score
-log10(Pvalue)
BP
CC
MF
KEGG
leukocyte mediated cytotoxicity
leukocyte mediated immunity
defense response to tumor cell
cell division
immune effector process
cytosol
anaphase-promoting complex
microtubule
immunological synapse
vesicle
CCR1 chemokine receptor binding
serine-type endopeptidase activity
anaphase-promoting complex binding
wide pore channel activity
ubiquitin conjugating enzyme activity
Apoptosis
Natural killer cell mediated cytotoxicity
Pyruvate metabolism
Mineral absorption
Cytosolic DNA-sensing pathway

Fig. 1 Overview of the integrative analysis workflow for identifying CDS-associated molecular subtypes and key genes in ccRCC.

Materials and Methods

Public data retrieval and preparation

Bulk transcriptomic and clinical data were assembled from ten public datasets. TCGA-KIRC RNA sequencing data included 538 ccRCC tumors and 72 non-tumor kidney samples and were obtained from the Genomic Data Commons. ICGC-RECA-EU data were obtained from the International Cancer Genome Consortium. The CheckMate dataset comprised pretreatment samples from advanced ccRCC trials of nivolumab (n = 181) or everolimus (n = 130) and was obtained from Braun et al. (2020)[17]. IMmotion150 expression and clinical data were retrieved through cBioPortal; the original trial included atezolizumab plus bevacizumab, atezolizumab monotherapy, and sunitinib arms[18]. CPTAC-ccRCC data were obtained from the Proteomic Data Commons (PDC000127). E-MTAB-1980 and E-MTAB-3267 were obtained from ArrayExpress; the E-MTAB-3267 cohort was reported by Beuselinck et al. (2015)[19]. GSE22541, GSE53757, and GSE40435 were obtained from the Gene Expression Omnibus; the original GSE22541 study was reported by Wuttig et al. (2012)[20]. Each cohort was analyzed separately. Dataset accessions, available sample counts, clinical endpoints, and treatment annotations are summarized in Online Resource 2, Table S1.

The single-cell RNA-sequencing dataset GSE156632 comprised seven ccRCC tumor specimens and five adjacent non-tumor specimens (Online Resource 2, Table S1)[21]. Samples were included in each analysis when the required clinical, expression, mutation, subtype, or response information was available. Samples without a matched CDS-cluster assignment or treatment-response record were omitted from the corresponding analysis. No new human specimens were collected.

Collection and scoring of cell death and senescence signatures

Twenty-one death- and senescence-associated gene signatures were compiled from the framework reported by Wang et al. (2025)[16], Reactome, Gene Ontology, FerrDb[22], and source publications. The collection

included cell-death pathways, autophagy-related modules, death-associated signaling, and senescence programs. Signature definitions, source identifiers, gene-set sizes, and constituent genes are provided in Online Resource 2, Table S2. Sample-level enrichment was quantified by single-sample gene set enrichment analysis (ssGSEA) implemented in the gene set variation analysis (GSVA) package[23]. Scores were calculated separately within each dataset.

Consensus clustering and gene-cluster analysis

Consensus clustering was performed independently within TCGA-KIRC, E-MTAB-1980, E-MTAB-3267, GSE22541, and IMmotion150 using the 21 CDS enrichment scores. ConsensusClusterPlus was run with 500 resampling iterations, pItem = 0.80, and pFeature = 1.00[24]. The number of clusters was evaluated from consensus matrices, cumulative distribution function curves, delta-area plots, and cluster stability; a three-cluster solution was used in each cohort. Cluster labels were assigned within each independently analyzed cohort. Principal component analysis used scaled scores and the base R prcomp function. Heatmaps were generated with ComplexHeatmap[25]. TCGA-KIRC CDS and gene-cluster assignments are listed in Online Resource 2, Table S3.

For TCGA-KIRC, subtype-specific differentially expressed genes (DEGs) were identified by comparing each CDS cluster with the other two clusters combined using limma[26]. Genes with an unadjusted $P < 0.05$ and absolute log2 fold change > 0.585 were retained, according to the implemented screening rule. The union of cluster-associated DEGs was subjected to consensus clustering with the same resampling parameters to define three gene clusters. Cluster-specific DEG lists and statistics are reported in Online Resource 2, Table S4.

Survival and pathway analyses

Kaplan-Meier curves and log-rank tests were used to compare time-to-event distributions. Overall survival (OS) was the endpoint in TCGA-KIRC, E-MTAB-1980, CPTAC, ICGC-RECA-EU, and CheckMate; progression-free survival (PFS) was used in E-MTAB-3267 and IMmotion150, and disease-free survival (DFS) in GSE22541 (Online Resource 2, Table S1). Cox proportional hazards regression was used for univariable and multivariable analyses. For continuous molecular variables, optimal cutoffs were selected with maxstat.

Time-dependent receiver operating characteristic curves were generated with timeROC. Functional enrichment was performed with clusterProfiler using Gene Ontology and Kyoto Encyclopedia of Genes and Genomes (KEGG) annotations[27]. Gene sets containing 5-5,000 genes were retained, and nominal $P < 0.05$ was used to select reported enrichment terms. Hallmark and KEGG pathway scores were estimated by GSVA[23]. Pairwise Mann-Whitney U tests and omnibus Kruskal-Wallis tests for GSVA scores are reported in Online Resource 2, Table S5.

Somatic mutation analysis

TCGA-KIRC somatic variants were obtained in mutation annotation format and processed with maftools[28]. The displayed 20-gene oncoplot was generated in SangerBox from the mutation-enriched subset containing at least one alteration in the displayed genes. PBRM1 and BAP1 status was summarized separately among samples with both mutation information and a matched CDS-cluster assignment.

Tumor microenvironment and immunotherapy-related analyses

Relative enrichment of 28 immune-cell signatures was estimated by ssGSEA using the gene sets reported by Charoentong et al. (2017)[29]. CIBERSORT was used as a complementary leukocyte deconvolution method[30], and ImmuCellAI was used to resolve T-cell-associated populations[31]. StromalScore, ImmuneScore, and ESTIMATEScore were calculated with ESTIMATE[32]. The T-cell-inflamed signature was calculated according to Ayers et al. (2017)[33]. Seven immunomodulator classes were obtained from a published pan-cancer immune resource[34]. Individual steps of the cancer-immunity cycle were scored by GSVA using the framework of Chen and Mellman (2013)[35].

For risk-group analyses, the Tumor Immune Dysfunction and Exclusion (TIDE) framework estimated dysfunction, exclusion, and predicted checkpoint-blockade response[36]. Subclass mapping (SubMap) compared high- and low-risk expression profiles with response profiles from a 47-patient melanoma immunotherapy dataset using 795 immune-related genes[37]. Nominal and Bonferroni-adjusted P values were reported.

Treatment-response analyses in external cohorts

The CDS consensus-clustering procedure was repeated independently in E-MTAB-3267, CheckMate, and IMmotion150 before response distributions were summarized. E-MTAB-3267 was analyzed as a sunitinib-treated cohort. Nivolumab and everolimus samples were pooled for the CheckMate descriptive analysis, and the atezolizumab plus bevacizumab, atezolizumab monotherapy, and sunitinib arms were pooled for IMmotion150. Response proportions were reported by locally assigned cluster.

Pharmacogenomic prediction and drug-target analysis

Drug-response resources were obtained from PRISM, the Genomics of Drug Sensitivity in Cancer (GDSC), and the Cancer Therapeutics Response Portal (CTRP). Curated overlap data were obtained through the Functional Data Consistency Explorer[38], and expression resources followed established cancer-cell-line datasets[39]. Drugs missing in more than 20% of cell lines and cell lines missing more than 50% of drugs were excluded. The filtered PRISM, CTRP, and GDSC datasets contained 479 cell lines/1,434 drugs, 845 cell lines/405 drugs, and 918 cell lines/285 drugs, respectively. Patient-level drug-response scores were predicted by ridge regression in oncoPredict[40]. Lower predicted response values were interpreted as greater predicted sensitivity, while retaining the metric supplied by the corresponding pharmacogenomic resource. For each subtype, candidates were identified by comparison with the other two subtypes combined; compounds with $P < 0.05$ in the corresponding comparison across all three resources were retained. The same framework was used to compare high- and low-risk groups. Annotations for the nine C2-associated candidate compounds are provided in Online Resource 2, Table S6.

Drug-target annotations for 7,540 compounds were obtained from the Drug Repurposing Hub release dated August 18, 2025[41]. After duplicate targets were removed, 2,430 unique targets remained. Ninety-five targets passing the study's expression filters were displayed across non-tumor tissue and CDS clusters. Target-level expression contrasts are provided in Online Resource 2, Table S7.

Edge perturbation matrix and node-gene prioritization

A sample-specific edge perturbation matrix was constructed from Reactome interactions using a rank-based procedure[42]. Expression values were ranked within each sample. For an edge connecting genes i and j in sample s, the edge rank difference was rank(i,s) minus rank(j,s). The normal reference was calculated from the ranks of mean gene expression across non-tumor samples. Each sample-specific perturbation was the difference between its edge rank difference and this normal reference. Absolute perturbation values were used to quantify perturbation intensity.

C2 was compared with C1 plus C3 using limma applied to absolute EPM values, with nominal $P < 0.05$. Stability was evaluated using 500 within-group bootstrap resamples with replacement (seed = 1234). Edges with boot_select_freq >= 0.60 and boot_direction_freq >= 0.50 were retained initially, giving 11,409 stable edges (Online Resource 2, Table S8). Ranking by absolute limma coefficient and applying abs_coef > 1,038 selected 1,711 edges, corresponding to approximately the top 15% of the stable-edge set. Requiring boot_select_freq = 1 and boot_direction_freq = 1 yielded 1,543 final differential edges. Their 721 distinct endpoint genes were summarized at node level. Nodes were retained when they participated in at least two selected edges and had C2_edge_ratio = 1, yielding 246 prioritized genes (Online Resource 2, Table S9). KEGG enrichment of these 246 genes is provided in Online Resource 2, Table S10.

Machine-learning prognostic model and clinical evaluation

Genes shared by the 246 network nodes and the 21 CDS gene sets were screened by univariable Cox regression in TCGA-KIRC. Twelve genes associated with overall survival were evaluated using 101 combinations constructed from CoxBoost, random survival forest (RSF), least absolute shrinkage and selection operator, ridge regression, elastic net, stepwise Cox regression, partial least-squares regression for Cox, supervised principal components, generalized boosted modeling, and survival support vector machine. TCGA-KIRC was used for model development. Model ranking was based on the mean concordance index across TCGA-KIRC, E-MTAB-1980, E-MTAB-3267, CPTAC, and GSE22541. The CoxBoost-plus-RSF pipeline with the highest five-cohort mean C-index was selected.

The final ten-gene model generated an individual risk score. Within each cohort, its survival outcomes were used by maxstat to determine the optimal cutoff for high- versus low-risk classification. The four cohorts outside TCGA-KIRC were used for external model evaluation. A nomogram combined the risk score with age, sex, stage, and grade in TCGA-KIRC. Calibration and decision curve analysis were performed in this cohort. Clinicopathological associations were evaluated using Wilcoxon rank-sum or Kruskal-Wallis tests, as appropriate. TCGA-KIRC risk-group annotations are included in Online Resource 2, Table S3.

Single-cell analysis and virtual knockout

GSE156632 was processed in Seurat[43]. Cells were retained when nFeature_RNA was 200-6,000, nCount_RNA was 200-40,000, and mitochondrial transcript percentage was <25%. Harmony was used for batch correction[44]. Clustering used the first 40 principal components and a resolution of 0.2, followed by UMAP visualization. Cell types were assigned from canonical markers, CellMarker 2.0[45], and published kidney-tumor annotations.

scTenifoldKnk was used to simulate LMNB1 and HSPA8 knockout in T cells and LY96 knockout in macrophages[46]. Genes with adjusted $P < 0.05$ were considered significantly perturbed. Perturbed genes were analyzed by Gene Ontology and KEGG enrichment.

Statistical analysis

Analyses were performed in R and GraphPad Prism 8.0.2. Paired tumor-normal expression comparisons used paired t tests; independent two-group comparisons used Wilcoxon rank-sum tests. Comparisons among multiple groups used one-way analysis of variance or Kruskal-Wallis tests, as described in the corresponding analyses. Kaplan-Meier curves were compared using log-rank tests. Figure 2 immune-score associations used Spearman correlations, whereas correlations of the prognostic score with CDS and immune signatures used Pearson correlations. Unadjusted $P < 0.05$ was used for limma differential-expression and edge screens, and adjusted $P < 0.05$ for scTenifoldKnk perturbation analysis. Enrichment tables retain both nominal and adjusted P values; the reported term screen used nominal $P < 0.05$.

Results

CDS transcriptional signatures exhibit distinct activity patterns and clinical associations in ccRCC

We assembled 21 gene signatures representing death- and senescence-associated programs and summarized their gene-set sizes(Fig. 2A; Online Resource 2, Table S2). The constituent genes showed extensive expression differences between ccRCC and non-tumor kidney tissues, revealing differences across multiple CDS signatures (Online Resource 1, Fig. S1A). ssGSEA further revealed broad interpatient variation in the enrichment of the 21 signatures across TCGA-KIRC and four external cohorts (Fig. 2B and Online Resource 1, Fig. S1B-E).

Comparison of 538 tumors with 72 non-tumor samples in TCGA-KIRC showed significant activity shifts for most CDS programs, with chaperone-mediated autophagy as the main exception (Fig. 2C). The direction of tumor-associated changes was largely reproduced in the paired GSE53757 and GSE40435 cohorts (Online Resource 1, Fig. S1F,G). These data support widespread but directionally heterogeneous remodeling of death- and senescence-associated transcriptional programs in ccRCC.

Univariable Cox analysis identified 12 CDS features associated with overall survival (Fig. 2D). Several inflammatory death and senescence programs were associated with higher mortality, whereas three features, including chaperone-mediated autophagy and entosis, showed favorable survival associations. Most CDS scores also correlated with ImmuneScore, StromalScore, ESTIMATEScore, and adaptive and innate immune-cell signatures (Fig. 2E). Inflammatory death and senescence programs generally tracked with immune infiltration, whereas several autophagy-related programs were inversely correlated.

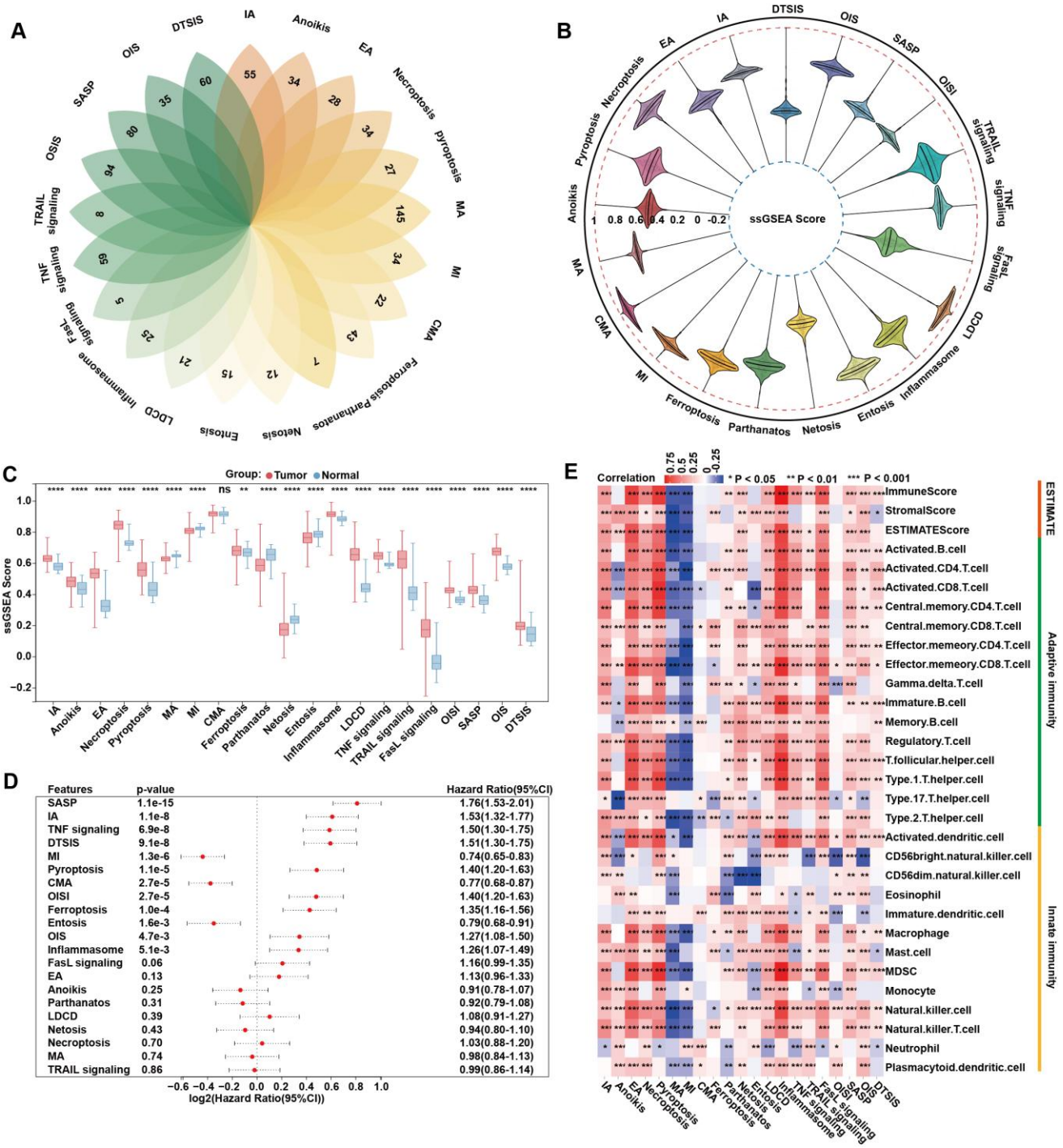


Fig. 2 Landscape and clinical relevance of cell death and senescence programs in ccRCC. (A) Petal plot showing the number of genes in each of the 21 CDS signatures. (B) Circular heatmap showing the distribution of CDS activity in TCGA-KIRC. (C) Comparison of CDS activity between 538 tumors and 72 non-tumor samples. (D) Univariable Cox analysis of CDS scores and overall survival. (E) Spearman correlations between CDS scores and tumor microenvironment/immune-cell measures. Red and blue indicate positive and negative correlations, respectively.

CDS-based clustering identifies three ccRCC subtypes with distinct survival outcomes and biological programs

Unsupervised consensus clustering based on the 21 CDS enrichment scores classified 538 TCGA-KIRC tumors into three subtypes: C1 (n = 156), C2 (n = 223), and C3 (n = 159) (Fig. 3A–C; Online Resource 1, Fig. S2A–C; Online Resource 2, Table S3). The subtypes differed significantly in T, N, and M categories, overall stage, and histological grade, whereas no significant differences were observed in age or sex (Fig. 3B). Overall survival differed significantly among the three subtypes (log-rank P = 0.00037), with C2 showing the poorest survival, C3 the most favorable survival, and C1 an intermediate outcome (Fig. 3D). All CDS enrichment scores except chaperone-mediated autophagy differed significantly across the subtypes (Fig. 3E). Concordantly, chaperone-mediated autophagy was likewise the main exception among CDS programs when tumor and non-tumor kidney tissues were compared

Applying consensus clustering separately to E-MTAB-3267, E-MTAB-1980, GSE22541, and IMmotion150 yielded three groups within each cohort, with distinct CDS activity profiles and differences in the available time-to-event outcomes (Online Resource 1, Figs. S2D–G and S3A–D). Group labels were assigned independently within each cohort.

Subtype-specific differential expression analysis identified 104 upregulated and 277 downregulated genes in C1, 474 upregulated and 99 downregulated genes in C2, and 274 upregulated and 285 downregulated genes in C3 (Fig. 3F; Online Resource 2, Table S4). Consensus clustering based on the expression of the combined subtype-associated genes further classified patients into three gene-expression subtypes, designated gene clusters A, B, and C (Fig. 3G–I; Online Resource 2, Table S3). Overall survival differed significantly among the gene clusters, with gene cluster B showing the poorest survival, gene cluster C the most favorable survival, and gene cluster A an intermediate outcome (log-rank P < 0.0001; Fig. 3H).

Pathway enrichment analysis further characterized the distinct biological programs associated with the three CDS subtypes. C1 was enriched for oxidative phosphorylation, peroxisome-related pathways, and MYC-, E2F-, and G2M-associated programs. C2 exhibited prominent enrichment of IL-6–JAK–STAT3, interferon, allograft rejection, JAK–STAT, NF-κB, TNF, cytokine–receptor interaction, and phagosome-related pathways. C3 was

characterized by enrichment of angiogenesis, hypoxia, WNT/β-catenin and Notch signaling, focal adhesion, extracellular matrix–receptor interaction, MAPK, PI3K–AKT, and RAP1 signaling (Fig. 3J; Online Resource 1, Fig. S3E; Online Resource 2, Table S5). Collectively, these findings delineated three CDS subtypes characterized by metabolic–proliferative, immune–inflammatory, and hypoxia–angiogenesis/adhesion-associated transcriptional profiles.

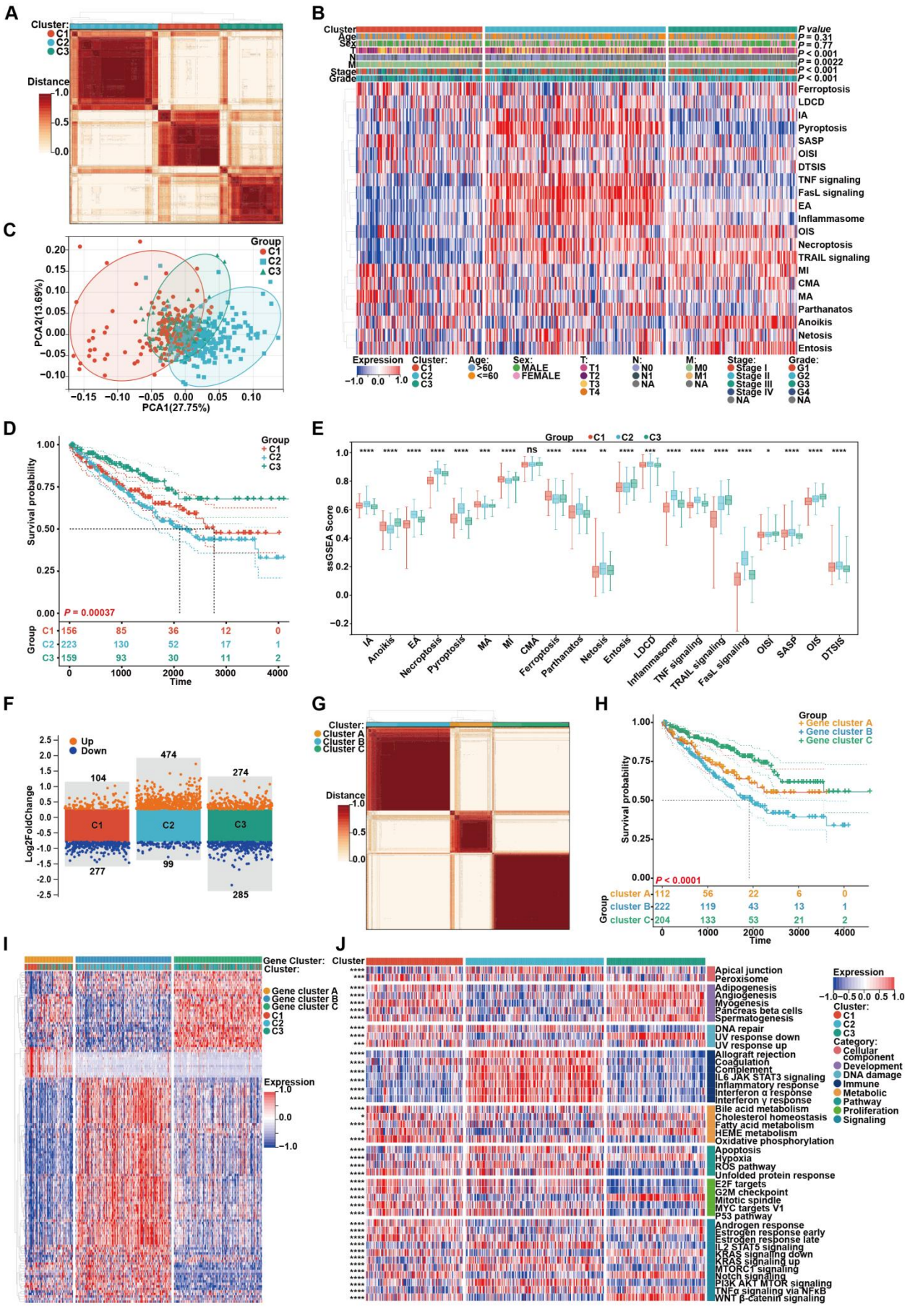

A
Cluster:
C1
C2
C3
Distance
1.0
0.5
0.0
B
Cluster
Age
Sex
T
N
M
Stage
Grade
P value
P = 0.31
P = 0.77
P < 0.0001
P = 0.0022
P < 0.001
P < 0.001
Ferroptosis
LDCD
IA
Pyroptosis
SASP
OISI
DTSIS
TNF signaling
FasL signaling
EA
Inflammasome
OIS
Necroptosis
TRAIL signaling
MI
CMA
MA
Parthanatos
Anoikis
Netosis
Entosis
Expression
Cluster:
Age:
>60
<=60
Sex:
MALE
FEMALE
T:
T1
T2
T3
T4
N:
N0
N1
NA
M:
M0
M1
NA
Stage:
Stage I
Stage II
Stage III
Stage IV
NA
Grade:
G1
G2
G3
G4
NA
C
Group
C1
C2
C3
PCA2(13.69%)
PCA1(27.75%)
D
Group
C1
C2
C3
Survival probability
P = 0.00037
Group
C1 156 85 36 12 0
C2 223 130 52 17 1
C3 159 93 30 11 2
Time
E
Group C1 C2 C3
ssGSEA Score
IA
Anoikis
EA
Necroptosis
Pyroptosis
MA
MI
CMA
Ferroptosis
Parthanatos
Netosis
Entosis
LDCD
Inflammasome
TNF signaling
TRAIL signaling
FasL signaling
OISI
SASP
OIS
DTSIS
F
Up
Down
Log2FoldChange
104
474
274
277
99
285
C1
C2
C3
G
Cluster:
Cluster A
Cluster B
Cluster C
Distance
H
Group
Gene cluster A
Gene cluster B
Gene cluster C
Survival probability
P < 0.0001
cluster A 112 56 22 6 0
cluster B 222 119 43 13 1
cluster C 204 133 53 21 2
Time
I
Gene Cluster:
Cluster:
Gene cluster A
Gene cluster B
Gene cluster C
C1
C2
C3
Expression
J
Cluster
Apical junction
Peroxisome
Adipogenesis
Angiogenesis
Myogenesis
Pancreas beta cells
Spermatogenesis
DNA repair
UV response down
UV response up
Allograft rejection
Coagulation
Complement
IL6 JAK STAT3 signaling
Inflammatory response
Interferon α response
Interferon γ response
Bile acid metabolism
Cholesterol homeostasis
Fatty acid metabolism
HEME metabolism
Oxidative phosphorylation
Apoptosis
Hypoxia
ROS pathway
Unfolded protein response
E2F targets
G2M checkpoint
Mitotic spindle
MYC targets V1
P53 pathway
Androgen response
Estrogen response early
Estrogen response late
IL2 STAT5 signaling
KRAS signaling down
KRAS signaling up
MTORC1 signaling
Notch signaling
PI3K AKT MTOR signaling
TNFα signaling via NFκB
WNT β-catenin signaling
Expression
Cluster:
C1
C2
C3
Category:
Cellular component
Development
DNA damage
Immune
Metabolic
Pathway
Proliferation
Signaling

Fig. 3 CDS-based classification and biological programs in TCGA-KIRC. (A) Consensus matrix for the three CDS clusters. (B) Heatmap of the 21 CDS scores with clinicopathological annotations. (C) Principal component analysis of CDS scores. (D) Kaplan-Meier overall-survival curves for C1, C2, and C3. (E) Differences in the 21 CDS scores among clusters. (F) Numbers of cluster-specific upregulated and downregulated genes. (G) Consensus matrix derived from CDS-cluster-associated DEGs. (H) Kaplan-Meier curves for gene clusters A-C. (I) Heatmap of the three gene clusters. (J) Hallmark GSVA profiles across CDS clusters.

The poor-prognosis C2 subtype exhibits immune-enriched and immunoregulatory features

Somatic mutation profiling identified VHL and PBRM1 among the most frequently altered genes in the displayed mutation-enriched subset, while subtype-stratified analysis revealed heterogeneous distributions of PBRM1 and BAP1 mutation status across the CDS subtypes (Fig. 4A,B).

Immune profiling revealed distinct features of C2. ssGSEA showed higher enrichment scores for multiple activated T-cell, B-cell, dendritic-cell, macrophage, and myeloid-cell signatures in C2, while CIBERSORT estimated additional differences in immune-cell composition (Fig. 4C and Online Resource 1, Fig. S4A,B). C2 also exhibited broadly increased expression of genes encoding co-stimulatory and co-inhibitory immune regulators, cytokines and their receptors, and molecules involved in antigen presentation and T-cell function (Fig. 4D). Moreover, C2 displayed the highest StromalScore, ImmuneScore, ESTIMATEScore, and T-cell-inflamed signature score (Fig. 4E–H).

Analysis of cancer-immunity cycle signatures revealed higher scores for immune-cell recruitment, infiltration, and tumor-cell recognition in C2, without a comparable increase in the tumor-cell-killing signature (step 7) (Online Resource 1, Fig. S4C). ImmuCellAI further indicated higher estimated representation of exhausted T cells and regulatory T-cell populations, including natural regulatory T cells, induced regulatory T cells, and type 1 regulatory T cells (Online Resource 1, Fig. S4D). Together with the poorer overall survival observed in C2, these findings suggest an immune-enriched transcriptional profile accompanied by prominent immunoregulatory features.

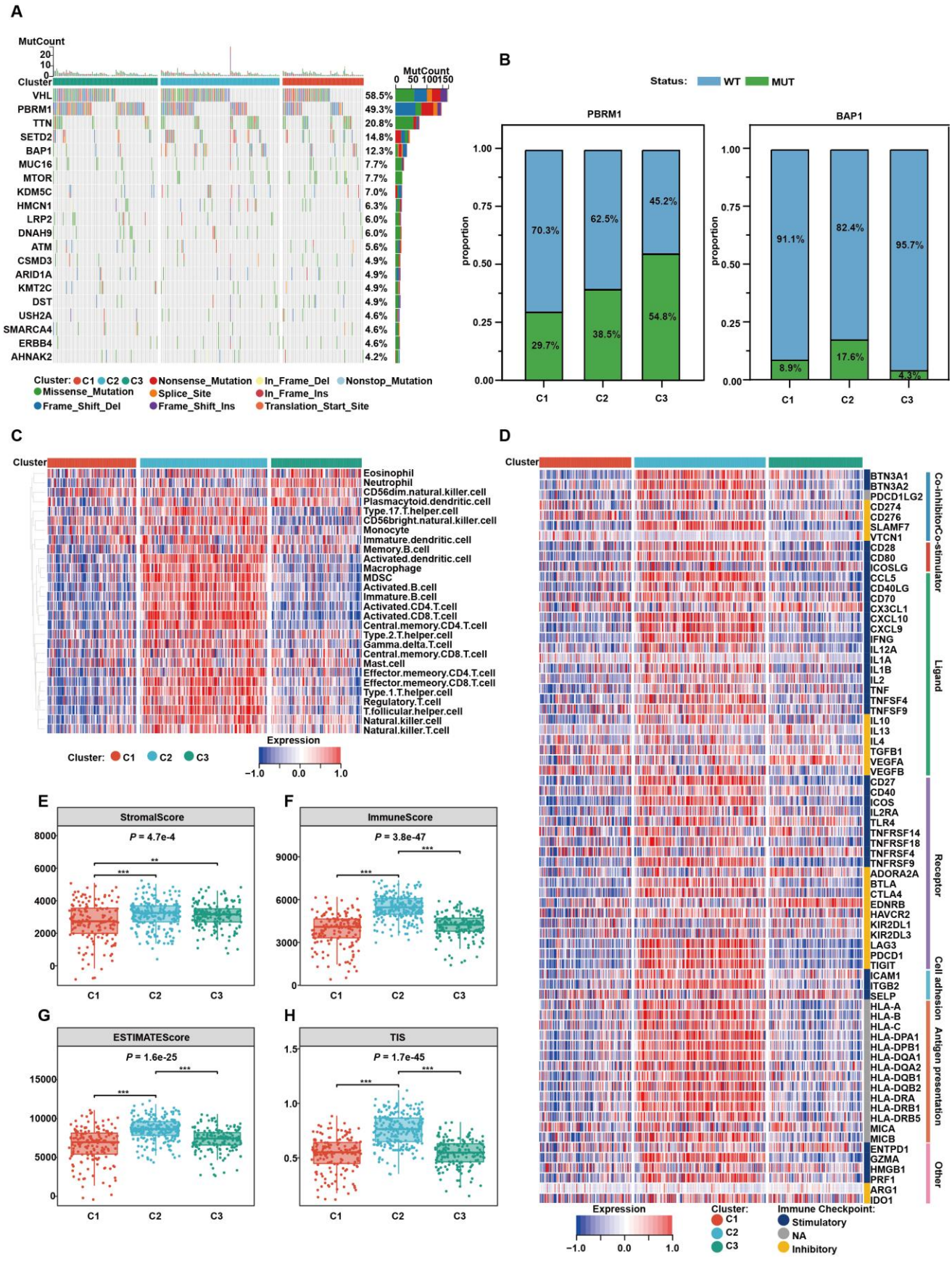

A
MutCount
Cluster
VHL 58.5%
PBRM1 49.3%
TTN 20.8%
SETD2 14.8%
BAP1 12.3%
MUC16 7.7%
MTOR 7.7%
KDM5C 7.0%
HMCN1 6.3%
LRP2 6.0%
DNAH9 6.0%
ATM 5.6%
CSMD3 4.9%
ARID1A 4.9%
KMT2C 4.9%
DST 4.9%
USH2A 4.6%
SMARCA4 4.6%
ERBB4 4.6%
AHNAK2 4.2%
Cluster: C1 C2 C3
Missense_Mutation
Frame_Shift_Del
Nonsense_Mutation
Splice_Site
Frame_Shift_Ins
In_Frame_Del
In_Frame_Ins
Translation_Start_Site
Nonstop_Mutation
B
Status: WT MUT
PBRM1
BAP1
proportion
70.3%
29.7%
62.5%
38.5%
45.2%
54.8%
91.1%
8.9%
82.4%
17.6%
95.7%
4.3%
C1 C2 C3
C
Cluster
Eosinophil
Neutrophil
CD56dim.natural.killer.cell
Plasmacytoid.dendritic.cell
Type.17.T.helper.cell
CD56bright.natural.killer.cell
Monocyte
Immature.dendritic.cell
Memory.B.cell
Activated.dendritic.cell
Macrophage
MDSC
Activated.B.cell
Immature.B.cell
Activated.CD4.T.cell
Activated.CD8.T.cell
Central.memory.CD4.T.cell
Type.2.T.helper.cell
Gamma.delta.T.cell
Central.memory.CD8.T.cell
Mast.cell
Effector.memeory.CD4.T.cell
Effector.memeory.CD8.T.cell
Type.1.T.helper.cell
Regulatory.T.cell
T.follicular.helper.cell
Natural.killer.cell
Natural.killer.T.cell
Cluster: C1 C2 C3
Expression
D
Cluster
BTN3A1
BTN3A2
PDCD1LG2
CD274
CD276
SLAMF7
VTCN1
CD28
CD80
ICOSLG
CCL5
CD40LG
CD70
CX3CL1
CXCL10
CXCL9
IFNG
IL12A
IL1A
IL1B
IL2
TNF
TNFSF4
TNFSF9
IL10
IL13
IL4
TGFB1
VEGFA
VEGFB
CD27
CD40
ICOS
IL2RA
TLR4
TNFRSF14
TNFRSF18
TNFRSF4
TNFRSF9
ADORA2A
BTLA
CTLA4
EDNRB
HAVCR2
KIR2DL1
KIR2DL3
LAG3
PDCD1
TIGIT
ICAM1
ITGB2
SELP
HLA-A
HLA-B
HLA-C
HLA-DPA1
HLA-DPB1
HLA-DQA1
HLA-DQA2
HLA-DQB1
HLA-DQB2
HLA-DRA
HLA-DRB1
HLA-DRB5
MICA
MICB
ENTPD1
GZMA
HMGB1
PRF1
ARG1
IDO1
Co-inhibitor
Co-stimulator
Ligand
Receptor
Cell adhesion
Antigen presentation
Other
Expression
Cluster: C1 C2 C3
Immune Checkpoint: Stimulatory NA Inhibitory
E
StromalScore
P = 4.7e-4
F
ImmuneScore
P = 3.8e-47
G
ESTIMATEScore
P = 1.6e-25
H
TIS
P = 1.7e-45
C1 C2 C3

Fig. 4 Mutation and immune landscapes of CDS clusters. (A) Oncoplot of recurrently altered genes in the displayed mutation-enriched TCGA-KIRC subset. (B) PBRM1 and BAP1 mutation status by CDS cluster among subtype-matched samples. (C) ssGSEA immune-cell enrichment heatmap. (D) Expression heatmap of immunomodulatory genes. (E-H) StromalScore, ImmuneScore, ESTIMATEScore, and T-cell-inflamed signature score across clusters. ns, not significant; *P < 0.05; **P <= 0.01; ***P <= 0.001; ****P <= 0.0001.

Predicted drug sensitivity of the poor-prognosis C2 subtype and treatment-response patterns in independent cohorts

To investigate the potential therapeutic vulnerabilities of the poor-prognosis C2 subtype, we used oncoPredict to estimate drug-response scores in TCGA-KIRC based on GDSC, CTRP, and PRISM pharmacogenomic resources (Fig. 5A). Comparison of C2 with the combined C1 and C3 groups identified nine compounds with differential predicted drug responses: AZD7762, AZD8055, BAM7, bosutinib, mitomycin C, nilotinib, PHA-793887, SNX-2112, and temozolomide (Fig. 5B; Online Resource 2, Table S6). These compounds targeted diverse mechanisms, including DNA-damage checkpoint kinases, mTOR, BAX, tyrosine kinases, cyclin-dependent kinases, HSP90, and DNA alkylation or crosslinking.

To further characterize the therapeutic target landscape, we examined the expression of 95 drug-associated genes curated from the Drug Repurposing Hub across C2, the other CDS subtypes, and non-tumor kidney tissues, revealing heterogeneous expression patterns (Fig. 5C; Online Resource 2, Table S7).

We next examined treatment-response patterns following independent CDS-based clustering in three therapeutic cohorts. In the sunitinib-treated E-MTAB-3267 cohort, the locally designated cluster 2 had the lowest responder proportion (11.1%), compared with 53.8% and 52.4% in clusters 1 and 3, respectively (Fig. 5D,E). Similarly, cluster 2 showed the lowest responder proportion in IMmotion150 (15.5% vs. 34.8% and 32.0%) and CheckMate (11.9% vs. 21.2% and 13.2%) (Fig. 5F–I). Cluster labels were assigned independently within each cohort.

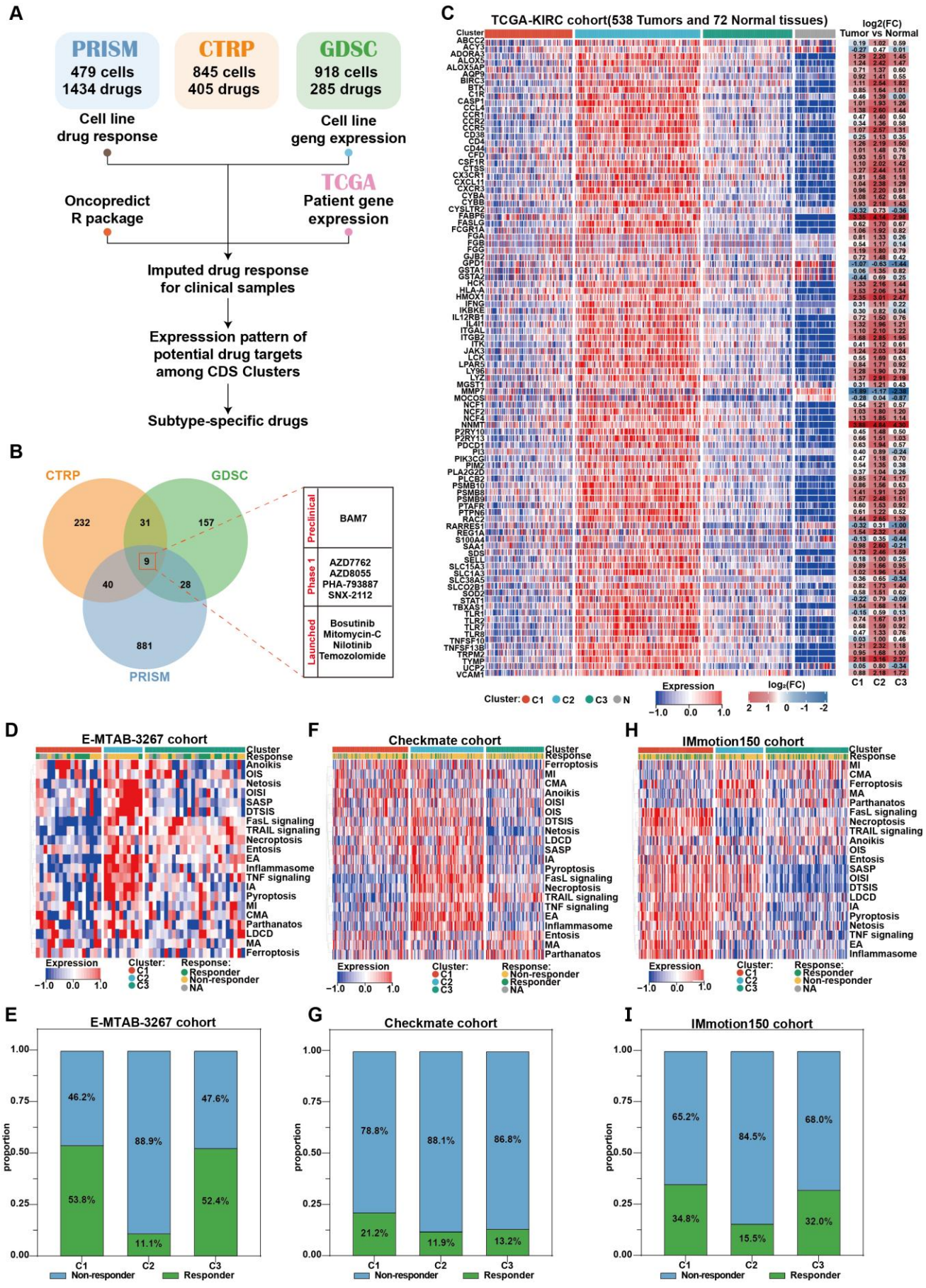

A
PRISM
479 cells
1434 drugs
CTRP
845 cells
405 drugs
GDSC
918 cells
285 drugs
Cell line drug response
Cell line geng expression
Oncopredict R package
TCGA
Patient gene expression
Imputed drug response for clinical samples
Expresssion pattern of potential drug targets among CDS Clusters
Subtype-specific drugs
B
CTRP
GDSC
PRISM
232
31
157
9
40
28
881
Preclinical
BAM7
Phase 1
AZD7762
AZD8055
PHA-793887
SNX-2112
Launched
Bosutinib
Mitomycin-C
Nilotinib
Temozolomide
C
TCGA-KIRC cohort(538 Tumors and 72 Normal tissues)
log2(FC)
Tumor vs Normal
Cluster: C1 C2 C3 N
Expression
log2(FC)
C1 C2 C3
D
E-MTAB-3267 cohort
Cluster
Response
Anoikis
OIS
Netosis
OISI
SASP
DTSIS
FasL signaling
TRAIL signaling
Necroptosis
Entosis
EA
Inflammasome
TNF signaling
IA
Pyroptosis
MI
CMA
Parthanatos
LDCD
MA
Ferroptosis
Expression
Cluster: C1 C2 C3
Response: Responder Non-responder NA
F
Checkmate cohort
Cluster
Response
Ferroptosis
MI
CMA
Anoikis
OISI
OIS
DTSIS
Netosis
LDCD
SASP
IA
Pyroptosis
FasL signaling
Necroptosis
TRAIL signaling
TNF signaling
EA
Inflammasome
Entosis
MA
Parthanatos
Expression
Cluster: C1 C2 C3
Response: Non-responder Responder NA
H
IMmotion150 cohort
Cluster
Response
MI
CMA
Ferroptosis
MA
Parthanatos
FasL signaling
Necroptosis
TRAIL signaling
Anoikis
OIS
Entosis
SASP
OISI
DTSIS
LDCD
IA
Pyroptosis
Netosis
TNF signaling
EA
Inflammasome
Expression
Cluster: C1 C2 C3
Response: Responder Non-responder NA
E
E-MTAB-3267 cohort
proportion
46.2%
53.8%
88.9%
11.1%
47.6%
52.4%
C1 C2 C3
Non-responder Responder
G
Checkmate cohort
proportion
78.8%
21.2%
88.1%
11.9%
86.8%
13.2%
C1 C2 C3
Non-responder Responder
I
IMmotion150 cohort
proportion
65.2%
34.8%
84.5%
15.5%
68.0%
32.0%
C1 C2 C3
Non-responder Responder

Fig. 5 Pharmacogenomic and treatment-response associations of CDS clusters. (A) Workflow for pharmacogenomic prediction. (B) Candidate compounds showing C2-associated predicted sensitivity across GDSC, CTRP, and PRISM. (C) Expression of 95 drug-associated genes across non-tumor tissue and CDS clusters, with subtype-versus-normal log2 fold changes. (D,E) E-MTAB-3267 cluster heatmap and sunitinib response proportions. (F,G) CheckMate cluster heatmap and pooled-arm response proportions. (H,I) IMmotion150 cluster heatmap and pooled-arm response proportions. Cluster labels were assigned independently within each treatment cohort; compound annotations and target-expression contrasts are provided in Online Resource 2, Tables S6-S7.

Edge perturbation analysis prioritizes CDS-related candidate genes in the poor-prognosis C2 subtype

To identify candidate network genes associated with the poor-prognosis C2 subtype, we constructed a sample-specific edge perturbation matrix (EPM) based on Reactome interactions and within-sample gene-expression ranks (Fig. 6A). For each directed interaction, the rank difference between connected genes was centered against a reference derived from ranked mean expression in non-tumor kidney samples. Analysis of 3,000 randomly sampled edges revealed greater and more broadly distributed perturbations in tumor tissues than in non-tumor samples, with varying perturbation intensities across the three CDS subtypes (Fig. 6B).

Focusing on C2 versus the combined C1 and C3 groups, initial statistical and bootstrap filtering identified 11,409 differential edges (Online Resource 2, Table S8). Applying an absolute edge-coefficient threshold of >1,038 retained 1,711 edges, representing approximately the top 15%. Further requiring 100% bootstrap selection frequency and consistent perturbation direction yielded 1,543 differential edges involving 721 unique endpoint genes. Subsequent node-level filtering prioritized 246 candidate genes (Fig. 6C,G; Online Resource 2, Table S9). Consensus clustering based on the selected differential edges revealed two network-defined groups that closely corresponded to the original C2 versus C1+C3 classification, as illustrated by PCA and heatmap analysis (Fig. 6D–F).

Network analysis identified several highly connected nodes, including ITGB2, HCK, KITLG, ITGAX, TNFSF13B, CD4, JAK3, LCP2, NCKAP1L, and PTPN6 (Fig. 6H). KEGG enrichment analysis of the 246 prioritized genes highlighted pathways involving regulation of the actin cytoskeleton, platelet activation, leukocyte transendothelial migration, Fc-gamma receptor-mediated phagocytosis, chemokine signaling, focal

adhesion, RAP1 signaling, T-cell receptor signaling, endocytosis, and MAPK signaling (Fig. 6I; Online Resource 2, Table S10). These enriched pathways were consistent with the immune-inflammatory features observed in C2. Intersecting the 246 candidate genes with the genes represented in the 21 CDS signatures yielded 23 CDS-related candidates, of which 12 were associated with overall survival in univariable Cox analysis (Fig. 6J,K).

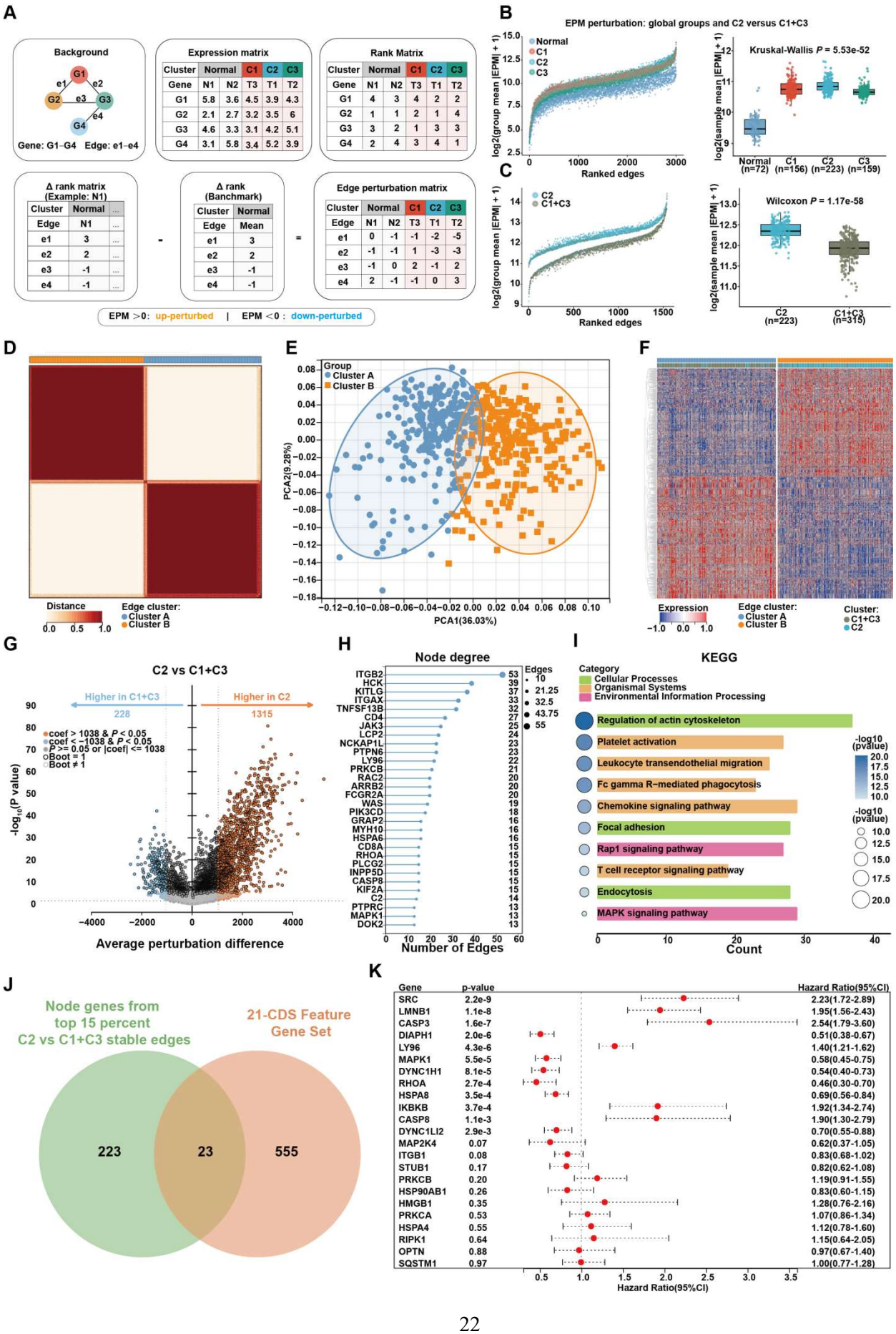

A
Background
Gene: G1–G4 Edge: e1–e4
Expression matrix
Rank Matrix
Δ rank matrix (Example: N1)
Δ rank (Banchmark)
Edge perturbation matrix
EPM >0: up-perturbed | EPM <0 : down-perturbed
B
EPM perturbation: global groups and C2 versus C1+C3
Normal
C1
C2
C3
log2(group mean |EPM| + 1)
Ranked edges
Kruskal-Wallis P = 5.53e-52
log2(sample mean |EPM| + 1)
Normal (n=72)
C1 (n=156)
C2 (n=223)
C3 (n=159)
C
C2
C1+C3
Wilcoxon P = 1.17e-58
C2 (n=223)
C1+C3 (n=315)
D
Distance
Edge cluster:
Cluster A
Cluster B
E
Group
Cluster A
Cluster B
PCA2(9.28%)
PCA1(36.03%)
F
Expression
Edge cluster:
Cluster:
C1+C3
C2
G
C2 vs C1+C3
Higher in C1+C3
228
Higher in C2
1315
coef > 1038 & P < 0.05
coef < −1038 & P < 0.05
P >= 0.05 or |coef| <= 1038
Boot = 1
Boot ≠ 1
-log10(P value)
Average perturbation difference
H
Node degree
Edges
10
21.25
32.5
43.75
55
ITGB2
HCK
KITLG
ITGAX
TNFSF13B
CD4
JAK3
LCP2
NCKAP1L
PTPN6
LY96
PRKCB
RAC2
ARRB2
FCGR2A
WAS
PIK3CD
GRAP2
MYH10
HSPA6
CD8A
RHOA
PLCG2
INPP5D
CASP8
KIF2A
C2
PTPRC
MAPK1
DOK2
Number of Edges
I
KEGG
Category
Cellular Processes
Organismal Systems
Environmental Information Processing
Regulation of actin cytoskeleton
Platelet activation
Leukocyte transendothelial migration
Fc gamma R−mediated phagocytosis
Chemokine signaling pathway
Focal adhesion
Rap1 signaling pathway
T cell receptor signaling pathway
Endocytosis
MAPK signaling pathway
-log10 (pvalue)
Count
J
Node genes from top 15 percent C2 vs C1+C3 stable edges
21-CDS Feature Gene Set
223
23
555
K
Gene
p-value
Hazard Ratio(95%CI)
SRC 2.2e-9 2.23(1.72-2.89)
LMNB1 1.1e-8 1.95(1.56-2.43)
CASP3 1.6e-7 2.54(1.79-3.60)
DIAPH1 2.0e-6 0.51(0.38-0.67)
LY96 4.3e-6 1.40(1.21-1.62)
MAPK1 5.5e-5 0.58(0.45-0.75)
DYNC1H1 8.1e-5 0.54(0.40-0.73)
RHOA 2.7e-4 0.46(0.30-0.70)
HSPA8 3.5e-4 0.69(0.56-0.84)
IKBKB 3.7e-4 1.92(1.34-2.74)
CASP8 1.1e-3 1.90(1.30-2.79)
DYNC1LI2 2.9e-3 0.70(0.55-0.88)
MAP2K4 0.07 0.62(0.37-1.05)
ITGB1 0.08 0.83(0.68-1.02)
STUB1 0.17 0.82(0.62-1.08)
PRKCB 0.20 1.19(0.91-1.55)
HSP90AB1 0.26 0.83(0.60-1.15)
HMGB1 0.35 1.28(0.76-2.16)
PRKCA 0.53 1.07(0.86-1.34)
HSPA4 0.55 1.12(0.78-1.60)
RIPK1 0.64 1.15(0.64-2.05)
OPTN 0.88 0.97(0.67-1.40)
SQSTM1 0.97 1.00(0.77-1.28)
Hazard Ratio(95%CI)

Fig. 6 Identification of candidate genes using sample-specific edge perturbation. (A) Construction of the edge perturbation matrix. (B) Perturbation intensity for 3,000 randomly selected edges in non-tumor tissue and CDS clusters. (C) Perturbation intensity for the selected top-15% stable C2-associated edges. (D) Consensus matrix defining two network states. (E) Principal component analysis of selected edges. (F) Heatmap of selected edge perturbations with CDS-cluster annotation. (G) Volcano plot showing the final 1,543 differential edges. (H) Thirty prioritized node genes with the highest edge connectivity. (I) KEGG enrichment of the 246 prioritized node genes. (J) Intersection of node genes with the 21 CDS signatures. (K) Univariable Cox analysis of the 23 intersecting genes.

Machine-learning integration identifies ten C2-associated CDS genes and establishes a prognostic signature

Building on the 12 survival-associated CDS candidates identified through C2-focused edge perturbation analysis, we evaluated 101 combinations of ten machine-learning algorithms to prioritize key genes and construct a prognostic model. Models were ranked according to the mean concordance index (C-index) across TCGA-KIRC, E-MTAB-1980, E-MTAB-3267, CPTAC, and GSE22541. The combination of CoxBoost and random survival forest (RSF) achieved the highest mean C-index (0.733) and selected ten genes: LMNB1, SRC, DYNC1H1, DIAPH1, RHOA, CASP3, IKBKB, LY96, HSPA8, and MAPK1 (Fig. 7A).

A prognostic risk score was subsequently derived from the ten-gene model. In TCGA-KIRC, increasing risk scores were accompanied by shorter survival times and more frequent death events. LMNB1, SRC, CASP3, IKBKB, and LY96 showed higher expression in the high-risk group, whereas DYNC1H1, DIAPH1, RHOA, HSPA8, and MAPK1 were more highly expressed in the low-risk group (Fig. 7B). High-risk patients exhibited significantly shorter overall survival ($P < 0.0001$; Fig. 7C), and the 1- to 5-year time-dependent AUCs ranged from 0.95 to 0.97 (Fig. 7D).

The prognostic performance of the selected model was further evaluated in four additional cohorts. Using cohort-specific maximally selected rank statistic (maxstat) cutoffs, high-risk patients showed less favorable survival outcomes in E-MTAB-1980, E-MTAB-3267, CPTAC, and GSE22541 ($P = 0.00047$, 0.0011, 0.0017, and 0.0031, respectively). The corresponding endpoints were OS, PFS, OS, and DFS (Online Resource 2, Table

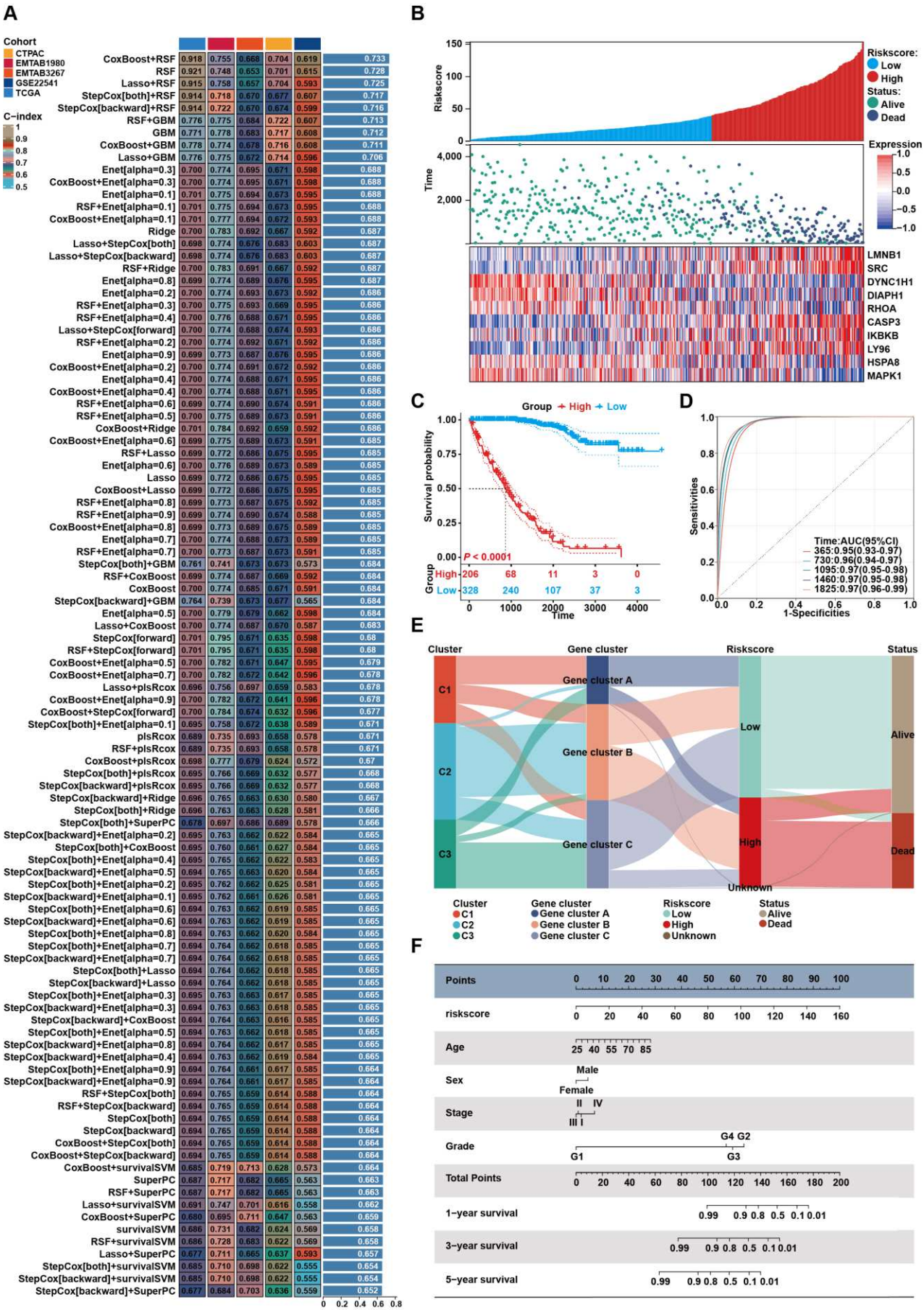
S1). Time-dependent AUCs ranged from 0.77 to 0.90, 0.69 to 0.78, 0.57 to 0.85, and 0.60 to 0.70, respectively (Online Resource 1, Fig. S5A–D).

The Sankey diagram illustrated the relationships among CDS subtype, gene cluster, risk group, and survival status (Fig. 7E; Online Resource 2, Table S3). A nomogram integrating the risk score with age, sex, stage, and grade showed agreement between predicted and observed survival probabilities and greater estimated net benefit than individual variables in TCGA-KIRC (Fig. 7F; Online Resource 1, Fig. S5E,F). High-risk status was associated with death events, advanced T, N, and M categories, higher stage, and higher histological grade, with risk scores increasing across unfavorable clinicopathological strata (Online Resource 1, Fig. S5G,H). Risk scores were also positively correlated with inflammatory apoptosis, pyroptosis, TNF signaling, the senescence-associated secretory phenotype (SASP), DNA-damage-induced senescence, and multiple immune-cell signatures (Online Resource 1, Fig. S5I,J).

To further characterize the immune features associated with the ten-gene signature, we compared the immune microenvironment between risk groups. The high-risk group exhibited higher ImmuneScore, ESTIMATEScore, and T-cell-inflamed signature scores, whereas StromalScore was comparable between groups (Online Resource 1, Fig. S6A–D). High-risk tumors also showed greater enrichment of exhausted and immunosuppressive cell-associated signatures, higher scores for several cancer-immunity-cycle steps, and increased PDCD1 (PD-1) and CTLA4 expression, but not CD274 (PD-L1) expression (Online Resource 1, Fig. S6E–I). Moreover, the high-risk group had higher TIDE and T-cell dysfunction scores and a lower computationally predicted immunotherapy response proportion than the low-risk group (28.6% vs. 40.9%; $P = 0.0042$; Online Resource 1, Fig. S6J–L). SubMap analysis showed nominal associations of high risk with a CTLA-4-response profile and low risk with a PD-1-response profile, although neither remained significant after Bonferroni correction (Online Resource 1, Fig. S6M).

Drug-sensitivity analysis further identified six compounds shared across CTRP, GDSC, and PRISM, four of which overlapped with the previously identified C2-associated candidates (Online Resource 1, Fig. S7A,B). Predicted drug-response profiles suggested greater sensitivity of the high-risk group to mitomycin C, AZD8055, SNX-2112, SAR-245409, and AZD7762, whereas PI-103 showed greater predicted sensitivity in the low-risk

403 group (Online Resource 1, Fig. S7C). Among commonly used renal cancer agents, the high-risk group exhibited
404 lower predicted drug-response values for sorafenib, cabozantinib, and pazopanib, while no significant
405 differences were observed for axitinib or sunitinib (Online Resource 1, Fig. S7D).


A
Cohort
CTPAC
EMTAB1980
EMTAB3267
GSE22541
TCGA
C−index
1
0.9
0.8
0.7
0.6
0.5
CoxBoost+RSF 0.918 0.755 0.668 0.704 0.619 0.733
RSF 0.921 0.748 0.653 0.701 0.615 0.728
Lasso+RSF 0.915 0.758 0.657 0.704 0.593 0.725
StepCox[both]+RSF 0.914 0.718 0.670 0.677 0.607 0.717
StepCox[backward]+RSF 0.914 0.722 0.670 0.674 0.599 0.716
RSF+GBM 0.776 0.775 0.684 0.722 0.607 0.713
GBM 0.771 0.778 0.683 0.717 0.608 0.712
CoxBoost+GBM 0.778 0.774 0.678 0.716 0.608 0.711
Lasso+GBM 0.776 0.775 0.672 0.714 0.596 0.706
Enet[alpha=0.3] 0.700 0.774 0.695 0.671 0.598 0.688
CoxBoost+Enet[alpha=0.3] 0.700 0.774 0.695 0.671 0.598 0.688
Enet[alpha=0.1] 0.701 0.775 0.694 0.673 0.595 0.688
RSF+Enet[alpha=0.1] 0.701 0.775 0.694 0.673 0.595 0.688
CoxBoost+Enet[alpha=0.1] 0.701 0.777 0.694 0.672 0.593 0.688
Ridge 0.700 0.783 0.692 0.667 0.592 0.687
Lasso+StepCox[both] 0.698 0.774 0.676 0.683 0.603 0.687
Lasso+StepCox[backward] 0.698 0.774 0.676 0.683 0.603 0.687
RSF+Ridge 0.700 0.783 0.691 0.667 0.592 0.687
Enet[alpha=0.8] 0.699 0.774 0.689 0.676 0.595 0.687
Enet[alpha=0.2] 0.700 0.774 0.693 0.673 0.592 0.686
RSF+Enet[alpha=0.3] 0.700 0.775 0.693 0.669 0.595 0.686
RSF+Enet[alpha=0.4] 0.700 0.776 0.688 0.671 0.595 0.686
Lasso+StepCox[forward] 0.700 0.774 0.688 0.674 0.593 0.686
RSF+Enet[alpha=0.2] 0.700 0.774 0.692 0.671 0.592 0.686
Enet[alpha=0.9] 0.699 0.773 0.687 0.676 0.595 0.686
CoxBoost+Enet[alpha=0.2] 0.700 0.774 0.691 0.672 0.592 0.686
Enet[alpha=0.4] 0.700 0.774 0.688 0.671 0.595 0.686
CoxBoost+Enet[alpha=0.4] 0.700 0.774 0.688 0.671 0.595 0.686
RSF+Enet[alpha=0.6] 0.699 0.774 0.690 0.674 0.591 0.686
RSF+Enet[alpha=0.5] 0.700 0.775 0.689 0.673 0.591 0.686
CoxBoost+Ridge 0.701 0.784 0.692 0.659 0.592 0.686
CoxBoost+Enet[alpha=0.6] 0.699 0.775 0.689 0.673 0.591 0.685
RSF+Lasso 0.699 0.772 0.686 0.675 0.595 0.685
Enet[alpha=0.6] 0.700 0.776 0.689 0.673 0.589 0.685
Lasso 0.699 0.772 0.686 0.675 0.595 0.685
CoxBoost+Lasso 0.699 0.772 0.686 0.675 0.595 0.685
RSF+Enet[alpha=0.8] 0.699 0.773 0.687 0.675 0.592 0.685
RSF+Enet[alpha=0.9] 0.699 0.774 0.690 0.674 0.588 0.685
CoxBoost+Enet[alpha=0.8] 0.699 0.773 0.689 0.675 0.589 0.685
Enet[alpha=0.7] 0.700 0.774 0.688 0.673 0.589 0.685
RSF+Enet[alpha=0.7] 0.700 0.773 0.687 0.673 0.591 0.685
StepCox[both]+GBM 0.761 0.741 0.673 0.673 0.573 0.684
RSF+CoxBoost 0.699 0.774 0.687 0.669 0.592 0.684
CoxBoost 0.700 0.774 0.685 0.671 0.591 0.684
StepCox[backward]+GBM 0.764 0.739 0.673 0.677 0.565 0.684
Enet[alpha=0.5] 0.700 0.779 0.679 0.662 0.598 0.684
Lasso+CoxBoost 0.700 0.774 0.687 0.670 0.587 0.683
StepCox[forward] 0.701 0.795 0.671 0.635 0.598 0.68
RSF+StepCox[forward] 0.701 0.795 0.671 0.635 0.598 0.68
CoxBoost+Enet[alpha=0.5] 0.700 0.782 0.671 0.647 0.595 0.679
CoxBoost+Enet[alpha=0.7] 0.700 0.782 0.672 0.642 0.596 0.678
Lasso+plsRcox 0.696 0.756 0.697 0.659 0.583 0.678
CoxBoost+Enet[alpha=0.9] 0.700 0.782 0.672 0.641 0.596 0.678
CoxBoost+StepCox[forward] 0.700 0.784 0.674 0.632 0.596 0.677
StepCox[both]+Enet[alpha=0.1] 0.695 0.758 0.672 0.638 0.589 0.671
plsRcox 0.689 0.735 0.693 0.658 0.578 0.671
RSF+plsRcox 0.689 0.735 0.693 0.658 0.578 0.671
CoxBoost+plsRcox 0.698 0.777 0.679 0.624 0.572 0.67
StepCox[both]+plsRcox 0.695 0.766 0.669 0.632 0.577 0.668
StepCox[backward]+plsRcox 0.695 0.766 0.669 0.632 0.577 0.668
StepCox[backward]+Ridge 0.696 0.765 0.663 0.630 0.580 0.667
StepCox[both]+Ridge 0.696 0.763 0.663 0.628 0.581 0.666
StepCox[both]+SuperPC 0.678 0.697 0.686 0.689 0.578 0.666
StepCox[backward]+Enet[alpha=0.2] 0.695 0.763 0.662 0.622 0.584 0.665
StepCox[both]+CoxBoost 0.695 0.760 0.661 0.627 0.584 0.665
StepCox[both]+Enet[alpha=0.4] 0.695 0.765 0.662 0.622 0.583 0.665
StepCox[backward]+Enet[alpha=0.5] 0.694 0.765 0.663 0.620 0.584 0.665
StepCox[both]+Enet[alpha=0.2] 0.695 0.762 0.662 0.625 0.581 0.665
StepCox[backward]+Enet[alpha=0.1] 0.695 0.762 0.661 0.626 0.581 0.665
StepCox[both]+Enet[alpha=0.6] 0.694 0.763 0.662 0.619 0.585 0.665
StepCox[backward]+Enet[alpha=0.6] 0.694 0.763 0.662 0.619 0.585 0.665
StepCox[both]+Enet[alpha=0.8] 0.694 0.763 0.662 0.620 0.584 0.665
StepCox[both]+Enet[alpha=0.7] 0.694 0.764 0.662 0.618 0.585 0.665
StepCox[backward]+Enet[alpha=0.7] 0.694 0.764 0.662 0.618 0.585 0.665
StepCox[both]+Lasso 0.694 0.764 0.662 0.618 0.585 0.665
StepCox[backward]+Lasso 0.694 0.764 0.662 0.618 0.585 0.665
StepCox[both]+Enet[alpha=0.3] 0.695 0.763 0.663 0.617 0.585 0.665
StepCox[backward]+Enet[alpha=0.3] 0.694 0.763 0.663 0.618 0.585 0.665
StepCox[backward]+CoxBoost 0.694 0.764 0.663 0.616 0.585 0.665
StepCox[both]+Enet[alpha=0.5] 0.694 0.763 0.662 0.618 0.585 0.665
StepCox[backward]+Enet[alpha=0.8] 0.694 0.764 0.662 0.617 0.585 0.665
StepCox[backward]+Enet[alpha=0.4] 0.694 0.763 0.662 0.619 0.584 0.665
StepCox[both]+Enet[alpha=0.9] 0.694 0.764 0.661 0.617 0.585 0.664
StepCox[backward]+Enet[alpha=0.9] 0.694 0.764 0.661 0.617 0.585 0.664
RSF+StepCox[both] 0.694 0.765 0.659 0.614 0.588 0.664
RSF+StepCox[backward] 0.694 0.765 0.659 0.614 0.588 0.664
StepCox[both] 0.694 0.765 0.659 0.614 0.588 0.664
StepCox[backward] 0.694 0.765 0.659 0.614 0.588 0.664
CoxBoost+StepCox[both] 0.694 0.765 0.659 0.614 0.588 0.664
CoxBoost+StepCox[backward] 0.694 0.765 0.659 0.614 0.588 0.664
CoxBoost+survivalSVM 0.685 0.719 0.713 0.628 0.573 0.664
SuperPC 0.687 0.717 0.682 0.665 0.563 0.663
RSF+SuperPC 0.687 0.717 0.682 0.665 0.563 0.663
Lasso+survivalSVM 0.691 0.747 0.701 0.616 0.558 0.662
CoxBoost+SuperPC 0.680 0.695 0.711 0.647 0.563 0.659
survivalSVM 0.686 0.731 0.682 0.624 0.569 0.658
RSF+survivalSVM 0.686 0.728 0.683 0.622 0.569 0.658
Lasso+SuperPC 0.677 0.711 0.665 0.637 0.593 0.657
StepCox[both]+survivalSVM 0.685 0.710 0.698 0.622 0.555 0.654
StepCox[backward]+survivalSVM 0.685 0.710 0.698 0.622 0.555 0.654
StepCox[backward]+SuperPC 0.677 0.684 0.703 0.636 0.559 0.652
0 0.2 0.4 0.6 0.8
B
Riskscore
150
100
50
0
Riskscore:
Low
High
Status:
Alive
Dead
Time
4,000
2,000
Expression
1.0
0.5
0.0
−0.5
−1.0
LMNB1
SRC
DYNC1H1
DIAPH1
RHOA
CASP3
IKBKB
LY96
HSPA8
MAPK1
C
Group High Low
Survival probability
1.00
0.75
0.50
0.25
0.00
P < 0.0001
Group
High 206 68 11 3 0
Low 328 240 107 37 3
0 1000 2000 3000 4000
Time
D
Sensitivities
1.0
0.8
0.6
0.4
0.2
0.0
Time:AUC(95%CI)
365:0.95(0.93-0.97)
730:0.96(0.94-0.97)
1095:0.97(0.95-0.98)
1460:0.97(0.95-0.98)
1825:0.97(0.96-0.99)
0.0 0.2 0.4 0.6 0.8 1.0
1-Specificities
E
Cluster
Gene cluster
Riskscore
Status
C1
C2
C3
Gene cluster A
Gene cluster B
Gene cluster C
Low
High
Unknown
Alive
Dead
Cluster
C1
C2
C3
Gene cluster
Gene cluster A
Gene cluster B
Gene cluster C
Riskscore
Low
High
Unknown
Status
Alive
Dead
F
Points 0 10 20 30 40 50 60 70 80 90 100
riskscore 0 20 40 60 80 100 120 140 160
Age 25 40 55 70 85
Sex
Male
Female
Stage
II IV
III I
Grade
G4 G2
G1 G3
Total Points 0 20 40 60 80 100 120 140 160 180 200
1−year survival 0.99 0.9 0.8 0.5 0.1 0.01
3−year survival 0.99 0.9 0.8 0.5 0.1 0.01
5−year survival 0.99 0.9 0.8 0.5 0.1 0.01

406

Fig. 7 Construction and evaluation of the CDS-related prognostic model. (A) Concordance indices for 101 machine-learning combinations across five cohorts and their mean values. (B) TCGA-KIRC risk-score distribution, survival status, and expression of the ten model genes. (C,D) Kaplan-Meier and time-dependent ROC analyses in TCGA-KIRC. (E) Sankey diagram linking CDS cluster, gene cluster, risk group, and survival status. (F) Nomogram integrating risk score and clinical variables to estimate 1-, 3-, and 5-year overall survival.

LMNB1, LY96, and HSPA8 exhibit distinct expression patterns and prognostic associations in ccRCC

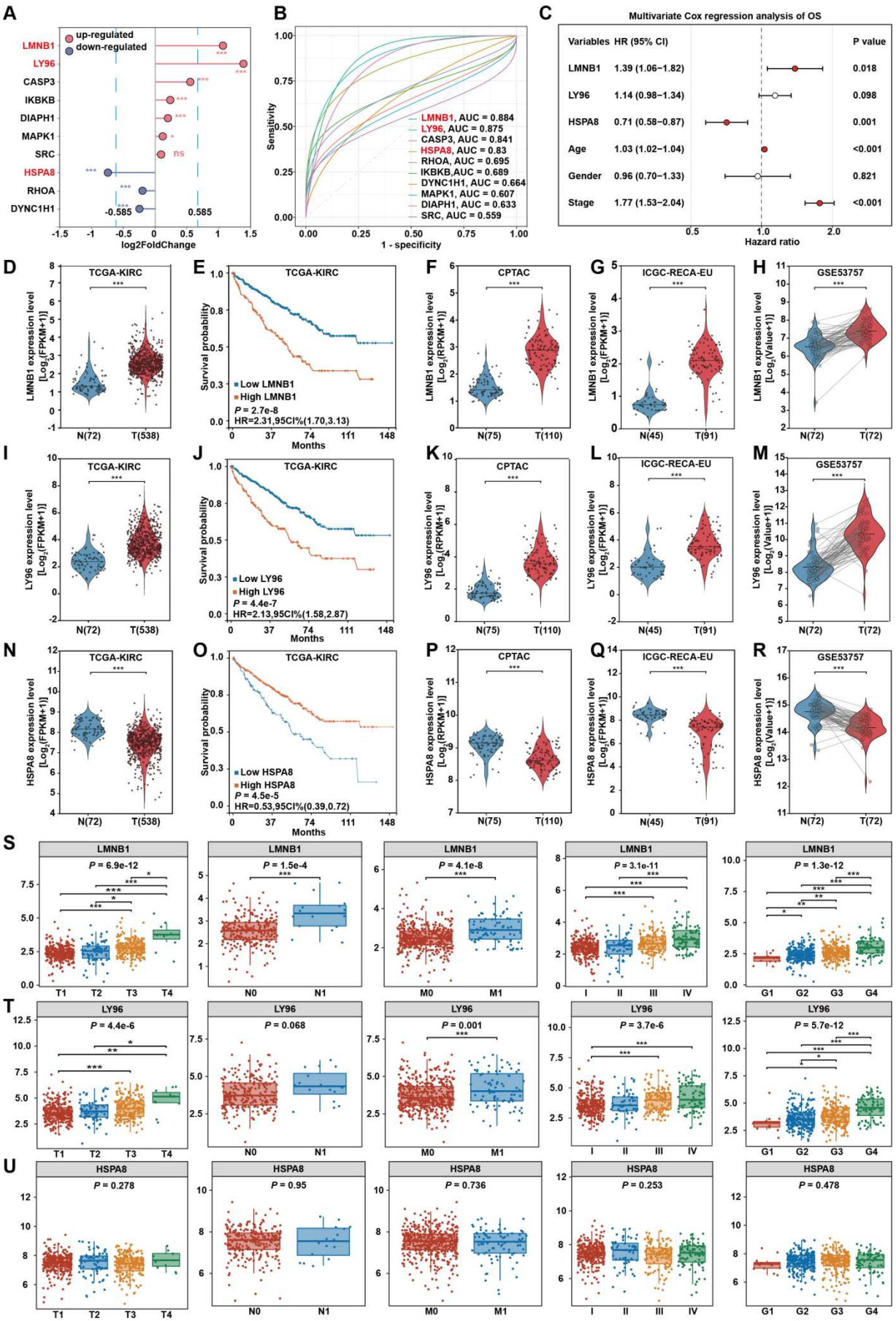
Among the ten genes included in the machine-learning prognostic signature, LMNB1, LY96, and HSPA8 were prioritized for further characterization based on their significant differential expression between ccRCC and non-tumor kidney tissues and their ranking among the top four genes by tumor-versus-non-tumor area under the curve (AUC). In TCGA-KIRC, LMNB1 and LY96 were upregulated in tumor tissues, whereas HSPA8 was downregulated (Fig. 8A). Receiver operating characteristic (ROC) analysis yielded AUCs of 0.884, 0.875, and 0.830 for LMNB1, LY96, and HSPA8, respectively (Fig. 8B).

Multivariable Cox regression incorporating the three genes and clinical covariates showed that higher LMNB1 expression was independently associated with shorter overall survival (HR = 1.39, 95% CI: 1.06–1.82; P = 0.018), whereas higher HSPA8 expression was associated with longer survival (HR = 0.71, 95% CI: 0.58–0.87; P = 0.001). LY96 did not retain statistical significance after adjustment (HR = 1.14, 95% CI: 0.98–1.34; P = 0.098) (Fig. 8C).

Consistent tumor-associated expression patterns were observed across TCGA-KIRC, CPTAC, ICGC-RECA-EU, and GSE53757, with higher LMNB1 and LY96 expression and lower HSPA8 expression in tumor tissues (Fig. 8D, F–H, I, K–M, and N, P–R). In TCGA-KIRC, higher LMNB1 and LY96 expression was associated with shorter overall survival, whereas higher HSPA8 expression was associated with longer survival (Fig. 8E,J,O). LMNB1 and LY96 expression levels were significantly associated with several adverse clinicopathological features, whereas HSPA8 showed no significant differences across these categories (Fig. 8S–U).

To further characterize the biological programs associated with these genes, we performed differential expression and pathway enrichment analyses. Genes differentially expressed according to LMNB1 or LY96

433 expression were enriched in pathways involving cytokine–receptor interactions, NF-κB, JAK–STAT, TNF
434 signaling, phagosome-related processes, cell adhesion, and metabolism (Online Resource 1, Fig. S8A–F; Online
435 Resource 2, Tables S11–S13). In the HSPA8-stratified analysis, genes classified as upregulated were enriched in
436 the tricarboxylic acid cycle, ferroptosis, and carbon metabolism, while glycolysis/gluconeogenesis reached
437 nominal significance ($P < 0.05$). Genes classified as downregulated were enriched in oxidative phosphorylation,
438 with additional nominal enrichment of glycerophospholipid metabolism, MAPK, RAS, and Notch signaling
439 pathways (Online Resource 1, Fig. S8G–I; Online Resource 2, Table S14).


A
up-regulated
down-regulated
LMNB1
LY96
CASP3
IKBKB
DIAPH1
MAPK1
SRC
HSPA8
RHOA
DYNC1H1
-0.585
0.585
log2FoldChange
B
Sensitivity
1 - specificity
LMNB1, AUC = 0.884
LY96, AUC = 0.875
CASP3, AUC = 0.841
HSPA8, AUC = 0.83
RHOA, AUC = 0.695
IKBKB,AUC = 0.689
DYNC1H1, AUC = 0.664
MAPK1, AUC = 0.607
DIAPH1, AUC = 0.633
SRC, AUC = 0.559
C
Multivariate Cox regression analysis of OS
Variables HR (95% CI) P value
LMNB1 1.39 (1.06−1.82) 0.018
LY96 1.14 (0.98−1.34) 0.098
HSPA8 0.71 (0.58−0.87) 0.001
Age 1.03 (1.02−1.04) <0.001
Gender 0.96 (0.70−1.33) 0.821
Stage 1.77 (1.53−2.04) <0.001
Hazard ratio
D
TCGA-KIRC
LMNB1 expression level [Log2(FPKM+1)]
N(72) T(538)
E
TCGA-KIRC
Survival probability
Low LMNB1
High LMNB1
P = 2.7e-8
HR=2.31,95CI%(1.70,3.13)
Months
F
CPTAC
LMNB1 expression level [Log2(RPKM+1)]
N(75) T(110)
G
ICGC-RECA-EU
LMNB1 expression level [Log2(FPKM+1)]
N(45) T(91)
H
GSE53757
LMNB1 expression level [Log2(Value+1)]
N(72) T(72)
I
TCGA-KIRC
LY96 expression level [Log2(FPKM+1)]
N(72) T(538)
J
TCGA-KIRC
Survival probability
Low LY96
High LY96
P = 4.4e-7
HR=2.13,95CI%(1.58,2.87)
Months
K
CPTAC
LY96 expression level [Log2(RPKM+1)]
N(75) T(110)
L
ICGC-RECA-EU
LY96 expression level [Log2(FPKM+1)]
N(45) T(91)
M
GSE53757
LY96 expression level [Log2(Value+1)]
N(72) T(72)
N
TCGA-KIRC
HSPA8 expression level [Log2(FPKM+1)]
N(72) T(538)
O
TCGA-KIRC
Survival probability
Low HSPA8
High HSPA8
P = 4.5e-5
HR=0.53,95CI%(0.39,0.72)
Months
P
CPTAC
HSPA8 expression level [Log2(RPKM+1)]
N(75) T(110)
Q
ICGC-RECA-EU
HSPA8 expression level [Log2(FPKM+1)]
N(45) T(91)
R
GSE53757
HSPA8 expression level [Log2(Value+1)]
N(72) T(72)
S
LMNB1
P = 6.9e-12
T1 T2 T3 T4
LMNB1
P = 1.5e-4
N0 N1
LMNB1
P = 4.1e-8
M0 M1
LMNB1
P = 3.1e-11
I II III IV
LMNB1
P = 1.3e-12
G1 G2 G3 G4
T
LY96
P = 4.4e-6
T1 T2 T3 T4
LY96
P = 0.068
N0 N1
LY96
P = 0.001
M0 M1
LY96
P = 3.7e-6
I II III IV
LY96
P = 5.7e-12
G1 G2 G3 G4
U
HSPA8
P = 0.278
T1 T2 T3 T4
HSPA8
P = 0.95
N0 N1
HSPA8
P = 0.736
M0 M1
HSPA8
P = 0.253
I II III IV
HSPA8
P = 0.478
G1 G2 G3 G4

440

Fig. 8 Expression and clinical characterization of LMNB1, LY96, and HSPA8. (A) Tumor-normal expression of the ten model genes in TCGA-KIRC. (B) Tumor-normal ROC analysis. (C) Multivariable Cox model including LMNB1, LY96, HSPA8, and clinical covariates. (D-H) LMNB1 expression in TCGA-KIRC, CPTAC, ICGC-RECA-EU, and GSE53757, with TCGA-KIRC survival analysis. (I-M) Corresponding analyses for LY96. (N-R) Corresponding analyses for HSPA8. (S-U) Associations of LMNB1, LY96, and HSPA8 expression with clinicopathological characteristics, including TNM classification, pathological stage, and histological grade in TCGA-KIRC.

Single-cell analysis reveals distinct cellular distributions and predicted functional associations of LMNB1, LY96, and HSPA8

To further characterize the cellular distribution and potential functions of LMNB1, LY96, and HSPA8, we analyzed single-cell RNA-seq data from GSE156632. Unsupervised clustering identified 22 transcriptional clusters, which were annotated into eight major cell populations: tumor cells, T/NK cells, proliferating T cells, monocytes, macrophages, mast cells, fibroblasts, and endothelial cells (Fig. 9A–C). LMNB1 showed relatively high expression in selected T-cell subsets, LY96 was predominantly expressed in macrophage and myeloid populations, and HSPA8 was broadly expressed across cell types, with relatively high expression in T-cell populations (Fig. 9D; Online Resource 1, Fig. S8J).

To explore their potential cell-type-associated functions, we performed virtual knockout analysis using scTenifoldKnk. Virtual knockout of LMNB1 in T cells identified 14 significantly perturbed genes, including H2AFZ, DPYSL2, PTTG1, PKM, and TUBA1C (Fig. 9E; Online Resource 1, Fig. S8K). Functional enrichment analysis linked these genes to leukocyte-mediated cytotoxicity, defense responses to tumor cells, immune-effector processes, natural killer cell-mediated cytotoxicity, apoptosis, and cytosolic DNA-sensing pathways (Fig. 9F).

Virtual knockout of LY96 in macrophages identified 11 significantly perturbed genes, including LTB, HLA-DRB5, HLA-DRB1, ENO1, and SPP1 (Fig. 9G; Online Resource 1, Fig. S8L). Enrichment analysis implicated interferon-γ signaling, antigen processing and presentation, MHC class II complexes, cytokine-mediated signaling, phagosome-related processes, T-helper-cell differentiation, and PI3K–AKT signaling (Fig. 9H). Similarly, virtual knockout of HSPA8 in T cells identified seven significantly perturbed

467 genes, including LTB, VIM, CCL4L2, FAM3C, and NUSAP1 (Fig. 9I; Online Resource 1, Fig. S8M). These
468 genes were associated with cytokine-mediated signaling, responses to cytokine stimulation, receptor regulation,
469 Toll-like receptor signaling, NF-κB signaling, chemokine signaling, and cytokine–receptor interactions (Fig.
470 9J).

471 Collectively, single-cell profiling and virtual knockout analyses linked LMNB1 to T-cell cytotoxicity- and
472 proliferation-related programs, LY96 to macrophage antigen presentation, and HSPA8 to T-cell cytokine
473 signaling. These findings provide a cellular perspective on the potential involvement of CDS-related genes in
474 immune microenvironment heterogeneity in ccRCC.

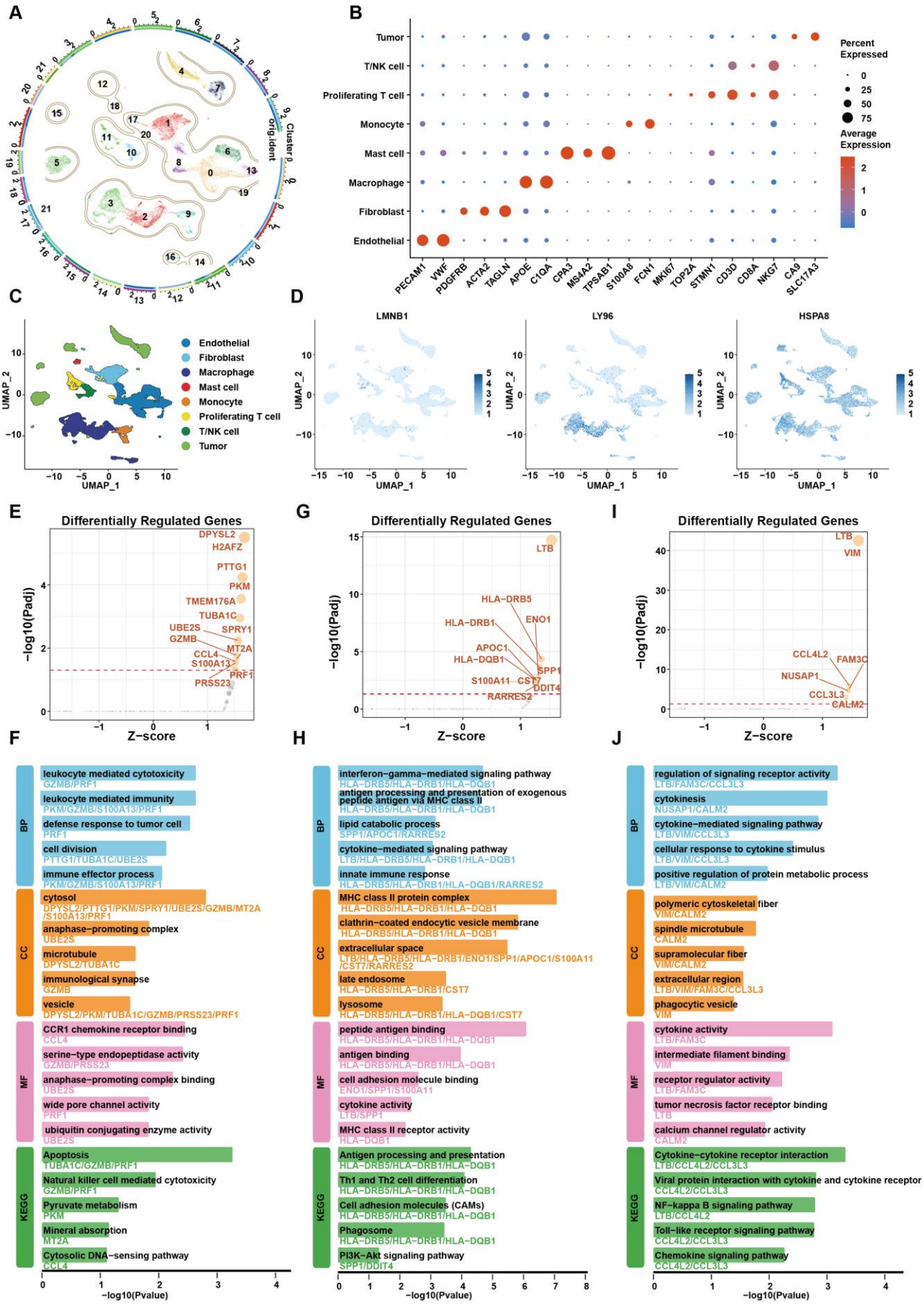

A
Cluster
orig.ident
B
Tumor
T/NK cell
Proliferating T cell
Monocyte
Mast cell
Macrophage
Fibroblast
Endothelial
PECAM1
VWF
PDGFRB
ACTA2
TAGLN
APOE
C1QA
CPA3
MSAA2
TPSAB1
S100A8
FCN1
MKI67
TOP2A
STMN1
CD3D
CD8A
NKG7
CA9
SLC17A3
Percent Expressed
Average Expression
C
Endothelial
Fibroblast
Macrophage
Mast cell
Monocyte
Proliferating T cell
T/NK cell
Tumor
UMAP_1
UMAP_2
D
LMNB1
LY96
HSPA8
E
Differentially Regulated Genes
DPYSL2
H2AFZ
PTTG1
PKM
TMEM176A
TUBA1C
UBE2S
SPRY1
GZMB
MT2A
CCL4
S100A13
PRF1
PRSS23
−log10(Padj)
Z−score
G
Differentially Regulated Genes
LTB
HLA−DRB5
HLA−DRB1
ENO1
APOC1
HLA−DQB1
SPP1
S100A11
CST7
DDIT4
RARRES2
I
Differentially Regulated Genes
LTB
VIM
CCL4L2
FAM3C
NUSAP1
CCL3L3
CALM2
F
BP
leukocyte mediated cytotoxicity
GZMB/PRF1
leukocyte mediated immunity
PKM/GZMB/S100A13/PRF1
defense response to tumor cell
PRF1
cell division
PTTG1/TUBA1C/UBE2S
immune effector process
PKM/GZMB/S100A13/PRF1
CC
cytosol
DPYSL2/PTTG1/PKM/SPRY1/UBE2S/GZMB/MT2A/S100A13/PRF1
anaphase−promoting complex
UBE2S
microtubule
DPYSL2/TUBA1C
immunological synapse
GZMB
vesicle
DPYSL2/PKM/TUBA1C/GZMB/PRSS23/PRF1
MF
CCR1 chemokine receptor binding
CCL4
serine−type endopeptidase activity
GZMB/PRSS23
anaphase−promoting complex binding
UBE2S
wide pore channel activity
PRF1
ubiquitin conjugating enzyme activity
UBE2S
KEGG
Apoptosis
TUBA1C/GZMB/PRF1
Natural killer cell mediated cytotoxicity
GZMB/PRF1
Pyruvate metabolism
PKM
Mineral absorption
MT2A
Cytosolic DNA−sensing pathway
CCL4
−log10(Pvalue)
H
BP
interferon−gamma−mediated signaling pathway
HLA−DRB5/HLA−DRB1/HLA−DQB1
antigen processing and presentation of exogenous peptide antigen via MHC class II
HLA−DRB5/HLA−DRB1/HLA−DQB1
lipid catabolic process
SPP1/APOC1/RARRES2
cytokine−mediated signaling pathway
LTB/HLA−DRB5/HLA−DRB1/HLA−DQB1
innate immune response
HLA−DRB5/HLA−DRB1/HLA−DQB1/RARRES2
CC
MHC class II protein complex
HLA−DRB5/HLA−DRB1/HLA−DQB1
clathrin−coated endocytic vesicle membrane
HLA−DRB5/HLA−DRB1/HLA−DQB1
extracellular space
LTB/HLA−DRB5/HLA−DRB1/ENO1/SPP1/APOC1/S100A11/CST7/RARRES2
late endosome
HLA−DRB5/HLA−DRB1/CST7
lysosome
HLA−DRB5/HLA−DRB1/HLA−DQB1/CST7
MF
peptide antigen binding
HLA−DRB5/HLA−DRB1/HLA−DQB1
antigen binding
HLA−DRB5/HLA−DRB1/HLA−DQB1
cell adhesion molecule binding
ENO1/SPP1/S100A11
cytokine activity
LTB/SPP1
MHC class II receptor activity
HLA−DQB1
KEGG
Antigen processing and presentation
HLA−DRB5/HLA−DRB1/HLA−DQB1
Th1 and Th2 cell differentiation
HLA−DRB5/HLA−DRB1/HLA−DQB1
Cell adhesion molecules (CAMs)
HLA−DRB5/HLA−DRB1/HLA−DQB1
Phagosome
HLA−DRB5/HLA−DRB1/HLA−DQB1
PI3K−Akt signaling pathway
SPP1/DDIT4
−log10(Pvalue)
J
BP
regulation of signaling receptor activity
LTB/FAM3C/CCL3L3
cytokinesis
NUSAP1/CALM2
cytokine−mediated signaling pathway
LTB/VIM/CCL3L3
cellular response to cytokine stimulus
LTB/VIM/CCL3L3
positive regulation of protein metabolic process
LTB/VIM/CALM2
CC
polymeric cytoskeletal fiber
VIM/CALM2
spindle microtubule
CALM2
supramolecular fiber
VIM/CALM2
extracellular region
LTB/VIM/FAM3C/CCL3L3
phagocytic vesicle
VIM
MF
cytokine activity
LTB/FAM3C
intermediate filament binding
VIM
receptor regulator activity
LTB/FAM3C
tumor necrosis factor receptor binding
LTB
calcium channel regulator activity
CALM2
KEGG
Cytokine−cytokine receptor interaction
LTB/CCL4L2/CCL3L3
Viral protein interaction with cytokine and cytokine receptor
CCL4L2/CCL3L3
NF−kappa B signaling pathway
LTB/CCL4L2
Toll−like receptor signaling pathway
CCL4L2/CCL3L3
Chemokine signaling pathway
CCL4L2/CCL3L3
−log10(Pvalue)

Fig. 9 Single-cell mapping and virtual knockout of LMNB1, LY96, and HSPA8. (A) UMAP of 22 transcriptional clusters from GSE156632. (B) Marker expression and positive-cell proportions for annotated populations. (C) UMAP of eight major cell types. (D) Single-cell expression maps for LMNB1, LY96, and HSPA8. (E,G,I) Global perturbation profiles after virtual knockout of LMNB1 in T cells, LY96 in macrophages, and HSPA8 in T cells, respectively. (F,H,J) Gene Ontology and KEGG enrichment of significantly perturbed genes for each virtual knockout.

Discussion

This study investigated the joint transcriptional organization of cell death and senescence (CDS) programs in ccRCC and its associations with molecular heterogeneity, immune microenvironment characteristics, and clinical outcomes. Three distinct CDS subtypes were identified, with the immune-enriched C2 subtype exhibiting the poorest prognosis. By integrating edge perturbation analysis with machine learning, we established a ten-gene prognostic signature and further characterized LMNB1, LY96, and HSPA8 through multicohort and single-cell analyses. These findings provide an integrated perspective on the relationship between CDS-associated molecular programs and ccRCC progression.

The biological heterogeneity of ccRCC is closely associated with alterations in VHL signaling, metabolic reprogramming, and interactions within the tumor microenvironment[4–6,47]. Previous studies have also demonstrated that VHL inactivation can induce cellular senescence, supporting the biological relevance of investigating senescence alongside cell death-associated processes[13]. In our study, CDS-based classification distinguished metabolic–proliferative, immune–inflammatory, and hypoxia–angiogenesis-associated transcriptional profiles. These findings extend previous investigations of CDS-related molecular heterogeneity in other malignancies[16] and suggest that the coordinated activities of cell death and senescence programs may capture distinct biological states in ccRCC.

A particularly notable finding was the coexistence of extensive immune infiltration and unfavorable survival in the C2 subtype. Although C2 exhibited elevated immune-cell infiltration and inflammatory signatures, it also showed enrichment of exhausted and regulatory T-cell-associated features without a corresponding increase in tumor-cell-killing signatures. These observations suggest that immune abundance alone may not adequately

reflect effective antitumor immunity. Previous studies have highlighted the contributions of dysfunctional T cells and immunosuppressive myeloid populations to ccRCC progression and treatment response[7,17,18]. Our findings further suggest that inflammatory CDS programs may be closely associated with the immunoregulatory characteristics of the ccRCC microenvironment, providing a potential explanation for the unfavorable prognosis of immune-enriched tumors.

To further characterize the molecular basis of the C2 phenotype, we applied edge perturbation analysis to identify network-associated genes. By incorporating relative expression relationships among interacting genes, this approach complements conventional differential expression analysis and provides additional information on molecular network organization[42]. The identified network genes were predominantly associated with immune regulation, leukocyte migration, cytoskeletal organization, and inflammatory signaling, consistent with the immune-inflammatory characteristics of C2. Subsequent integration with CDS gene signatures and machine-learning algorithms yielded a ten-gene prognostic model. The associations of this signature with survival, clinicopathological characteristics, and immune-related programs suggest that network-associated CDS genes may capture clinically relevant aspects of ccRCC heterogeneity.

Among the identified genes, LMNB1, LY96, and HSPA8 exhibited distinct expression patterns, prognostic associations, and cellular distributions. LMNB1 encodes a major component of the nuclear lamina and has been implicated in chromatin organization, cellular proliferation, and senescence. Previous studies have associated elevated LMNB1 expression with aggressive features and unfavorable outcomes in ccRCC[48,49]. Interestingly, Lamin-B1 depletion is also recognized as a characteristic of classical cellular senescence[50], suggesting that its biological significance may depend on cellular context. Consistent with its potential involvement in proliferative and immune-related processes, our single-cell analysis revealed relatively high LMNB1 expression in selected T-cell populations, while virtual perturbation implicated cytotoxicity- and proliferation-associated programs. These observations highlight the potential relevance of LMNB1 to the interplay between CDS-related cellular states and immune regulation in ccRCC.

LY96 encodes MD-2, an essential component of the TLR4 signaling complex involved in innate immune recognition and inflammatory responses[51,52]. Its increased expression and association with inflammatory

pathways were consistent with the immune-enriched characteristics of C2. Single-cell analysis further localized LY96 predominantly to macrophage and myeloid populations, while virtual perturbation implicated antigen presentation, MHC class II-associated processes, and cytokine signaling. Although LY96 was associated with overall survival in single-gene analysis, its association was not independently significant after adjustment for clinical covariates and the other selected genes. Together, these findings suggest that LY96 may represent an inflammation-associated molecular feature linking CDS-related heterogeneity with myeloid immune regulation in ccRCC.

In contrast, HSPA8 exhibited lower expression in ccRCC tissues, while higher expression was associated with more favorable survival. HSPA8 is a constitutive HSP70-family chaperone involved in protein homeostasis, stress adaptation, and chaperone-mediated autophagy, with context-dependent functions across malignancies[47,53–55]. Notably, the gene-level associations of HSPA8 contrasted with the relatively stable chaperone-mediated autophagy signature across CDS subtypes, suggesting that individual pathway components may provide biological information beyond aggregate pathway activity. Furthermore, its associations with metabolic pathways and T-cell cytokine-related signaling indicate a potential connection between protein homeostasis, cellular stress responses, and immune regulation in ccRCC.

Pharmacogenomic analyses additionally identified candidate compounds targeting cell-cycle regulation, mTOR signaling, molecular chaperones, and other stress-related pathways. Several compounds were shared between the C2-associated and prognostic risk-group analyses, suggesting partial convergence of their predicted therapeutic sensitivity profiles. Differences in treatment-response proportions among CDS-defined groups in independent therapeutic cohorts further indicated potential clinical relevance. These observations provide a basis for investigating whether CDS-associated molecular states could inform therapeutic stratification and the identification of candidate treatment strategies in ccRCC.

Although our findings provide insights into CDS-associated heterogeneity in ccRCC, several limitations should be acknowledged. Our study primarily relied on publicly available cohorts, which, despite encompassing multiple datasets, may not fully represent the clinical and molecular diversity of ccRCC. Potential sex-specific differences also warrant further investigation. Moreover, the biological functions of the identified candidate

genes and the therapeutic potential of the predicted compounds require further experimental confirmation. Future cell-based and animal studies, together with prospective clinical validation, will help clarify their mechanistic and translational significance.

Conclusion

In conclusion, our study highlights the associations of CDS-related transcriptional programs with molecular heterogeneity, immune regulation, and prognosis in ccRCC. The integration of network analysis, machine learning, and single-cell profiling identified LMNB1, LY96, and HSPA8 as promising candidates for further investigation, providing new insights into the interplay between cellular stress responses and the tumor immune microenvironment.

Abbreviations

ccRCC clear cell renal cell carcinoma

CDS cell death- and senescence-associated

TCGA The Cancer Genome Atlas

KIRC Kidney Renal Clear Cell Carcinoma

ICGC International Cancer Genome Consortium

CPTAC Clinical Proteomic Tumor Analysis Consortium

GEO Gene Expression Omnibus

OS overall survival

PFS progression-free survival

DFS disease-free survival

HR hazard ratio

CI confidence interval

ROC receiver operating characteristic

AUC area under the curve

C-index concordance index

DEGs differentially expressed genes

ssGSEA single-sample gene set enrichment analysis

GSVA gene set variation analysis

GO Gene Ontology

KEGG Kyoto Encyclopedia of Genes and Genomes

EPM edge perturbation matrix

RSF random survival forest

LASSO least absolute shrinkage and selection operator

Enet elastic net

SVM support vector machine

GBM generalized boosted model

SuperPC supervised principal components

TME tumor microenvironment

TIDE Tumor Immune Dysfunction and Exclusion

ICI immune checkpoint inhibitor

CNV copy number variation

SNV single nucleotide variation

MAF mutation annotation format

GDSC Genomics of Drug Sensitivity in Cancer

CTRP Cancer Therapeutics Response Portal

PRISM Profiling Relative Inhibition Simultaneously in Mixtures

Data Availability

No new sequencing data were generated. All bulk and single-cell datasets analyzed in this study are publicly available from the repositories and accession identifiers described in Materials and Methods.

Statements and Declarations

Author contributions

W.X.Y: Data curation,Conception and design, Formal analysis, Methodology, Writing—original draft, Visualization, Validation. H.H: Data collection, Data analysis， Writing - original draft,Visualization. W.K.H:Conceptualization, Project administration, Reviewing and Editing. All authors have read and agreed to the published version of the manuscript.

Funding

No funding.

Ethics approval

Not applicable.

Consent for publication

Not applicable.

Conflicts of interest

The authors declare no competing interests.

Competing interests

The authors declared no competing interest.

Clinical trial number

Not applicable.

References

1. Hsieh JJ, Purdue MP, Signoretti S, Swanton C, Albiges L, Schmidinger M, et al. Renal cell carcinoma. Nat Rev Dis Primer. 2017;3:17009. https://doi.org/10.1038/nrdp.2017.9

2. Rose TL, Kim WY. Renal Cell Carcinoma: A Review. JAMA. 2024;332:1001. https://doi.org/10.1001/jama.2024.12848

3. The Cancer Genome Atlas Research Network. Comprehensive molecular characterization of clear cell renal cell carcinoma. Nature. 2013;499:43–9. https://doi.org/10.1038/nature12222

4. Gerlinger M, Rowan AJ, Horswell S, Larkin J, Endesfelder D, Gronroos E, et al. Intratumor Heterogeneity and Branched Evolution Revealed by Multiregion Sequencing. N Engl J Med. 2012;366:883–92. https://doi.org/10.1056/NEJMoa1113205

5. Sato Y, Yoshizato T, Shiraishi Y, Maekawa S, Okuno Y, Kamura T, et al. Integrated molecular analysis of clear-cell renal cell carcinoma. Nat Genet. 2013;45:860–7. https://doi.org/10.1038/ng.2699

6. Vuong L, Kotecha RR, Voss MH, Hakimi AA. Tumor Microenvironment Dynamics in Clear-Cell Renal Cell Carcinoma. Cancer Discov. 2019;9:1349–57. https://doi.org/10.1158/2159-8290.CD-19-0499

7. Bi K, He MX, Bakouny Z, Kanodia A, Napolitano S, Wu J, et al. Tumor and immune reprogramming during immunotherapy in advanced renal cell carcinoma. Cancer Cell. 2021;39:649-661.e5. https://doi.org/10.1016/j.ccell.2021.02.015

8. Galluzzi L, Vitale I, Aaronson SA, Abrams JM, Adam D, Agostinis P, et al. Molecular mechanisms of cell death: recommendations of the Nomenclature Committee on Cell Death 2018. Cell Death Differ. 2018;25:486–541. https://doi.org/10.1038/s41418-017-0012-4

9. Bedoui S, Herold MJ, Strasser A. Emerging connectivity of programmed cell death pathways and its physiological implications. Nat Rev Mol Cell Biol. 2020;21:678–95. https://doi.org/10.1038/s41580-020-0270-8

10. Gorgoulis V, Adams PD, Alimonti A, Bennett DC, Bischof O, Bishop C, et al. Cellular Senescence: Defining a Path Forward. Cell. 2019;179:813–27. https://doi.org/10.1016/j.cell.2019.10.005

11. Fane M, Weeraratna AT. How the ageing microenvironment influences tumour progression. Nat Rev Cancer. 2020;20:89–106. https://doi.org/10.1038/s41568-019-0222-9

12. Childs BG, Baker DJ, Kirkland JL, Campisi J, Van Deursen JM. Senescence and apoptosis: dueling or complementary cell fates? EMBO Rep. 2014;15:1139–53. https://doi.org/10.15252/embr.201439245

13. Young AP, Schlisio S, Minamishima YA, Zhang Q, Li L, Grisanzio C, et al. VHL loss actuates a HIF-independent senescence programme mediated by Rb and p400. Nat Cell Biol. 2008;10:361–9. https://doi.org/10.1038/ncb1699

14. Jiang S, Dong Y, Wang J, Zhang X, Liu W, Wei Y, et al. Identification of immunogenic cell death-related signature on prognosis and immunotherapy in kidney renal clear cell carcinoma. Front Immunol. 2023;14:1207061. https://doi.org/10.3389/fimmu.2023.1207061

15. Fei C, Zhen X, Shiqiang Z, Jun P. Frontier knowledge and future directions of programmed cell death in clear cell renal cell carcinoma. Cell Death Discov. 2024;10:113. https://doi.org/10.1038/s41420-024-01880-0

16. Wang P, Zhang C, Wu P, Zhao Z, Sun N, Xue Q, et al. Cell Death and Senescence-Based Molecular Classification and an Individualized Prediction Model for Lung Adenocarcinoma. MedComm. 2025;6:e70237. https://doi.org/10.1002/mco2.70237

17. Braun DA, Hou Y, Bakouny Z, Ficial M, Sant' Angelo M, Forman J, et al. Interplay of somatic alterations and immune infiltration modulates response to PD-1 blockade in advanced clear cell renal cell carcinoma. Nat Med. 2020;26:909–18. https://doi.org/10.1038/s41591-020-0839-y

18. McDermott DF, Huseni MA, Atkins MB, Motzer RJ, Rini BI, Escudier B, et al. Clinical activity and molecular correlates of response to atezolizumab alone or in combination with bevacizumab versus sunitinib in renal cell carcinoma. Nat Med. 2018;24:749–57. https://doi.org/10.1038/s41591-018-0053-3

19. Beuselinck B, Job S, Becht E, Karadimou A, Verkarre V, Couchy G, et al. Molecular Subtypes of Clear Cell Renal Cell Carcinoma Are Associated with Sunitinib Response in the Metastatic Setting. Clin Cancer Res. 2015;21:1329–39. https://doi.org/10.1158/1078-0432.CCR-14-1128

20. Wuttig D, Zastrow S, Füssel S, Toma MI, Meinhardt M, Kalman K, et al. CD31, EDNRB and TSPAN7 are promising prognostic markers in clear-cell renal cell carcinoma revealed by genome-wide expression analyses of primary tumors and metastases. Int J Cancer [Internet]. 2012 [cited 2026 Oct 13];131. https://doi.org/10.1002/ijc.27419

21. Zhang M, Zhai W, Miao J, Cheng X, Luo W, Song W, et al. Single cell analysis reveals intra-tumour heterogeneity, microenvironment and potential diagnosis markers for clear cell renal cell carcinoma. Clin Transl Med. 2022;12:e713. https://doi.org/10.1002/ctm2.713

22. Zhou N, Bao J. FerrDb: a manually curated resource for regulators and markers of ferroptosis and ferroptosis-disease associations. Database. 2020;2020:baaa021. https://doi.org/10.1093/database/baaa021

23. Hänzelmann S, Castelo R, Guinney J. GSVA: gene set variation analysis for microarray and RNA-Seq data. BMC Bioinformatics. 2013;14:7. https://doi.org/10.1186/1471-2105-14-7

24. Wilkerson MD, Hayes DN. ConsensusClusterPlus: a class discovery tool with confidence assessments and item tracking. Bioinformatics. 2010;26:1572–3. https://doi.org/10.1093/bioinformatics/btq170

25. Gu Z, Eils R, Schlesner M. Complex heatmaps reveal patterns and correlations in multidimensional genomic data. Bioinformatics. 2016;32:2847–9. https://doi.org/10.1093/bioinformatics/btw313

26. Ritchie ME, Phipson B, Wu D, Hu Y, Law CW, Shi W, et al. limma powers differential expression analyses for RNA-sequencing and microarray studies. Nucleic Acids Res. 2015;43:e47–e47. https://doi.org/10.1093/nar/gkv007

27. Yu G, Wang L-G, Han Y, He Q-Y. clusterProfiler: an R Package for Comparing Biological Themes Among Gene Clusters. OMICS J Integr Biol. 2012;16:284–7. https://doi.org/10.1089/omi.2011.0118

28. Mayakonda A, Lin D-C, Assenov Y, Plass C, Koeffler HP. Maftools: efficient and comprehensive analysis of somatic variants in cancer. Genome Res. 2018;28:1747–56. https://doi.org/10.1101/gr.239244.118

29. Charoentong P, Finotello F, Angelova M, Mayer C, Efremova M, Rieder D, et al. Pan-cancer Immunogenomic Analyses Reveal Genotype-Immunophenotype Relationships and Predictors of Response to Checkpoint Blockade. Cell Rep. 2017;18:248–62. https://doi.org/10.1016/j.celrep.2016.12.019

30. Newman AM, Liu CL, Green MR, Gentles AJ, Feng W, Xu Y, et al. Robust enumeration of cell subsets from tissue expression profiles. Nat Methods. 2015;12:453–7. https://doi.org/10.1038/nmeth.3337

31. Miao Y, Zhang Q, Lei Q, Luo M, Xie G, Wang H, et al. ImmuCellAI: A Unique Method for Comprehensive T-Cell Subsets Abundance Prediction and its Application in Cancer Immunotherapy. Adv Sci. 2020;7:1902880. https://doi.org/10.1002/advs.201902880

32. Yoshihara K, Shahmoradgoli M, Martínez E, Vegesna R, Kim H, Torres-Garcia W, et al. Inferring tumour purity and stromal and immune cell admixture from expression data. Nat Commun. 2013;4:2612. https://doi.org/10.1038/ncomms3612

33. Ayers M, Lunceford J, Nebozhyn M, Murphy E, Loboda A, Kaufman DR, et al. IFN-γ–related mRNA profile predicts clinical response to PD-1 blockade. J Clin Invest. 2017;127:2930–40. https://doi.org/10.1172/JCI91190

34. Thorsson V, Gibbs DL, Brown SD, Wolf D, Bortone DS, Ou Yang T-H, et al. The Immune Landscape of Cancer. Immunity. 2018;48:812-830.e14. https://doi.org/10.1016/j.immuni.2018.03.023

35. Chen DS, Mellman I. Oncology Meets Immunology: The Cancer-Immunity Cycle. Immunity. 2013;39:1–10. https://doi.org/10.1016/j.immuni.2013.07.012

36. Fu J, Li K, Zhang W, Wan C, Zhang J, Jiang P, et al. Large-scale public data reuse to model immunotherapy response and resistance. Genome Med. 2020;12:21. https://doi.org/10.1186/s13073-020-0721-z

37. Hoshida Y, Brunet J-P, Tamayo P, Golub TR, Mesirov JP. Subclass Mapping: Identifying Common Subtypes in Independent Disease Data Sets. Hofmann O, editor. PLoS ONE. 2007;2:e1195. https://doi.org/10.1371/journal.pone.0001195

38. Cai L, Liu H, Minna JD, DeBerardinis RJ, Xiao G, Xie Y. Assessing consistency across functional screening datasets in cancer cells. Kendziorski C, editor. Bioinformatics. 2021;37:4540–7. https://doi.org/10.1093/bioinformatics/btab423

719 39. Iorio F, Knijnenburg TA, Vis DJ, Bignell GR, Menden MP, Schubert M, et al. A Landscape of
720 Pharmacogenomic Interactions in Cancer. Cell. 2016;166:740–54. https://doi.org/10.1016/j.cell.2016.06.017

721 40. Maeser D, Gruener RF, Huang RS. oncoPredict: an R package for predicting *in vivo* or cancer patient drug
722 response and biomarkers from cell line screening data. Brief Bioinform. 2021;22:bbab260.
723 https://doi.org/10.1093/bib/bbab260

724 41. Corsello SM, Bittker JA, Liu Z, Gould J, McCarren P, Hirschman JE, et al. The Drug Repurposing Hub: a
725 next-generation drug library and information resource. Nat Med. 2017;23:405–8.
726 https://doi.org/10.1038/nm.4306

727 42. Chen Y, Gu Y, Hu Z, Sun X. Sample-specific perturbation of gene interactions identifies breast cancer
728 subtypes. Brief Bioinform. 2021;22:bbaa268. https://doi.org/10.1093/bib/bbaa268

729 43. Stuart T, Butler A, Hoffman P, Hafemeister C, Papalexi E, Mauck WM, et al. Comprehensive Integration of
730 Single-Cell Data. Cell. 2019;177:1888-1902.e21. https://doi.org/10.1016/j.cell.2019.05.031

731 44. Korsunsky I, Millard N, Fan J, Slowikowski K, Zhang F, Wei K, et al. Fast, sensitive and accurate integration
732 of single-cell data with Harmony. Nat Methods. 2019;16:1289–96. https://doi.org/10.1038/s41592-019-0619-0

733 45. Hu C, Li T, Xu Y, Zhang X, Li F, Bai J, et al. CellMarker 2.0: an updated database of manually curated cell
734 markers in human/mouse and web tools based on scRNA-seq data. Nucleic Acids Res. 2023;51:D870–6.
735 https://doi.org/10.1093/nar/gkac947

736 46. Osorio D, Zhong Y, Li G, Xu Q, Yang Y, Tian Y, et al. scTenifoldKnk: An efficient virtual knockout tool for
737 gene function predictions via single-cell gene regulatory network perturbation. Patterns. 2022;3:100434.
738 https://doi.org/10.1016/j.patter.2022.100434

739 47. Liao W, Huang M, Du X, Tang L, Li J, Tang Q. Comprehensive analysis of heat shock protein 110, 90, 70,
740 60 families and tumor immune microenvironment characterization in clear cell renal cell carcinoma. Sci Rep.
741 2025;15:469. https://doi.org/10.1038/s41598-024-84834-x

48. Radspieler M, Schindeldecker M, Stenzel P, Försch S, Tagscherer K, Herpel E, et al. Lamin-B1 is a senescence-associated biomarker in clear-cell renal cell carcinoma. Oncol Lett [Internet]. 2019 [cited 2026 Oct 13]; https://doi.org/10.3892/ol.2019.10593

49. Qin H, Lu Y, Du L, Shi J, Yin H, Jiang B, et al. Pan-cancer analysis identifies LMNB1 as a target to redress Th1/Th2 imbalance and enhance PARP inhibitor response in human cancers. Cancer Cell Int. 2022;22:101. https://doi.org/10.1186/s12935-022-02467-4

50. Freund A, Laberge R-M, Demaria M, Campisi J. Lamin B1 loss is a senescence-associated biomarker. Magin TM, editor. Mol Biol Cell. 2012;23:2066–75. https://doi.org/10.1091/mbc.e11-10-0884

51. Nie K, Li J, Peng L, Zhang M, Huang W. Pan-Cancer Analysis of the Characteristics of LY96 in Prognosis and Immunotherapy Across Human Cancer. Front Mol Biosci. 2022;9:837393. https://doi.org/10.3389/fmolb.2022.837393

52. Heine H, Zamyatina A. Therapeutic Targeting of TLR4 for Inflammation, Infection, and Cancer: A Perspective for Disaccharide Lipid A Mimetics. Pharmaceuticals. 2022;16:23. https://doi.org/10.3390/ph16010023

53. Liu J, Wang L, He H, Liu Y, Jiang Y, Yang J. The Complex Role of Chaperone-Mediated Autophagy in Cancer Diseases. Biomedicines. 2023;11:2050. https://doi.org/10.3390/biomedicines11072050

54. Kou X, Yang X, Zhao Z, Li L. HSPA8-mediated stability of the CLPP protein regulates mitochondrial autophagy in cisplatin-resistant ovarian cancer cells. Acta Biochim Biophys Sin [Internet]. 2024 [cited 2026 Oct 13]; https://doi.org/10.3724/abbs.2023246

55. Ruzza A, Zaltron E, Vianello F, Celotti I, Scavezzon M, Severin F, et al. HSPA8 and HSPA9: Two prognostic and therapeutic targets in breast, colon, and kidney cancers? Biochim Biophys Acta BBA - Mol Basis Dis. 2025;1871:167827. https://doi.org/10.1016/j.bbadis.2025.167827

765 Online Resource 1 Supplementary figure legends

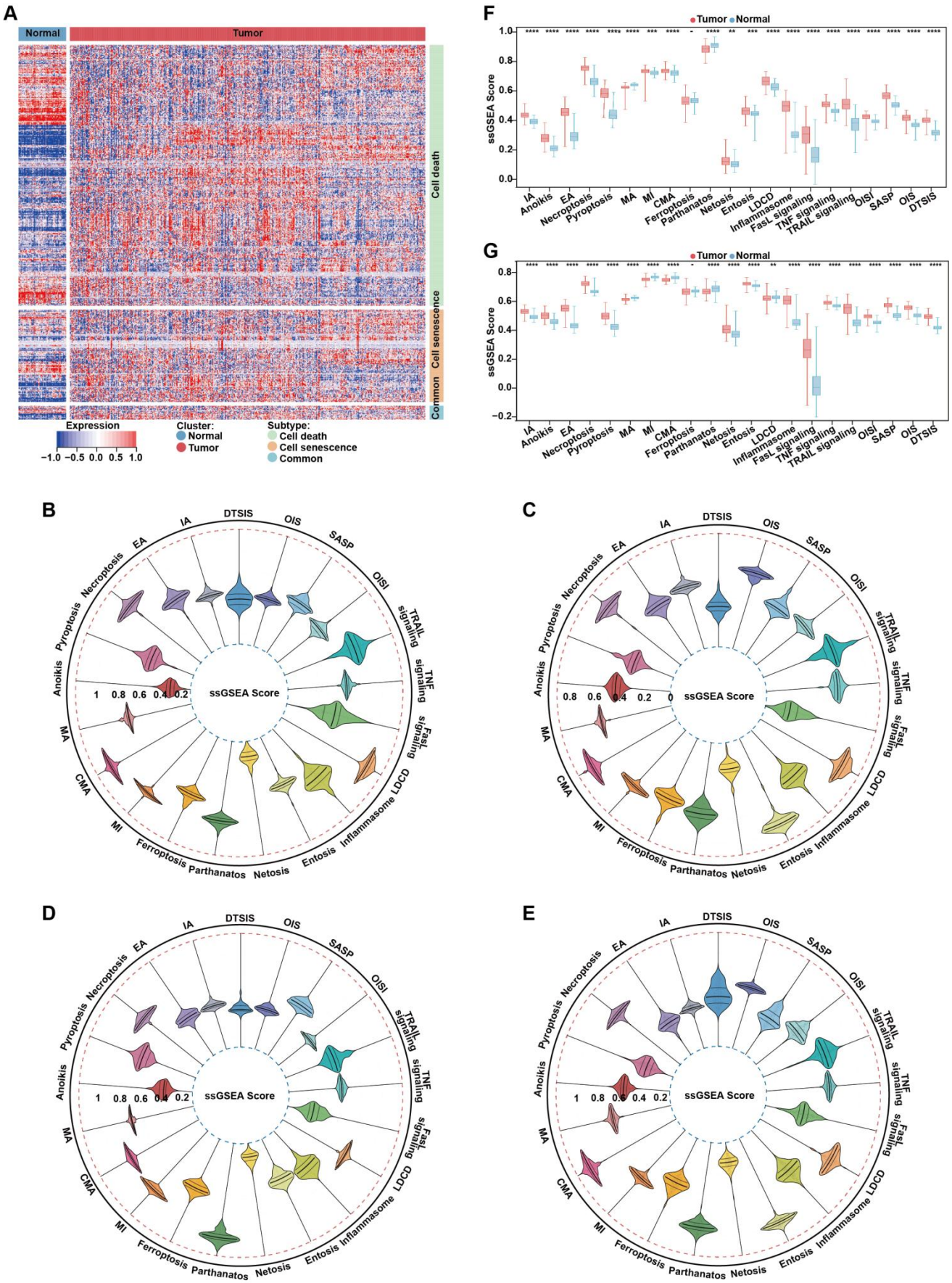

A
Normal
Tumor
Cell death
Cell senescence
Common
Expression
−1.0 −0.5 0.0 0.5 1.0
Cluster:
Normal
Tumor
Subtype:
Cell death
Cell senescence
Common
F
Tumor Normal
ssGSEA Score
IA
Anoikis
EA
Necroptosis
Pyroptosis
MA
MI
CMA
Ferroptosis
Parthanatos
Netosis
Entosis
LDCD
Inflammasome
FasL signaling
TNF signaling
TRAIL signaling
OISI
SASP
OIS
DTSIS
G
Tumor Normal
ssGSEA Score
B
C
D
E
ssGSEA Score

Fig. S1 Expression and activity of CDS programs across datasets. (A) Expression heatmap of CDS-signature genes in TCGA-KIRC. (B-E) CDS activity distributions in E-MTAB-3267, E-MTAB-1980, GSE22541, and IMmotion150. (F,G) Tumor-normal CDS activity comparisons in paired GSE53757 and GSE40435 samples.

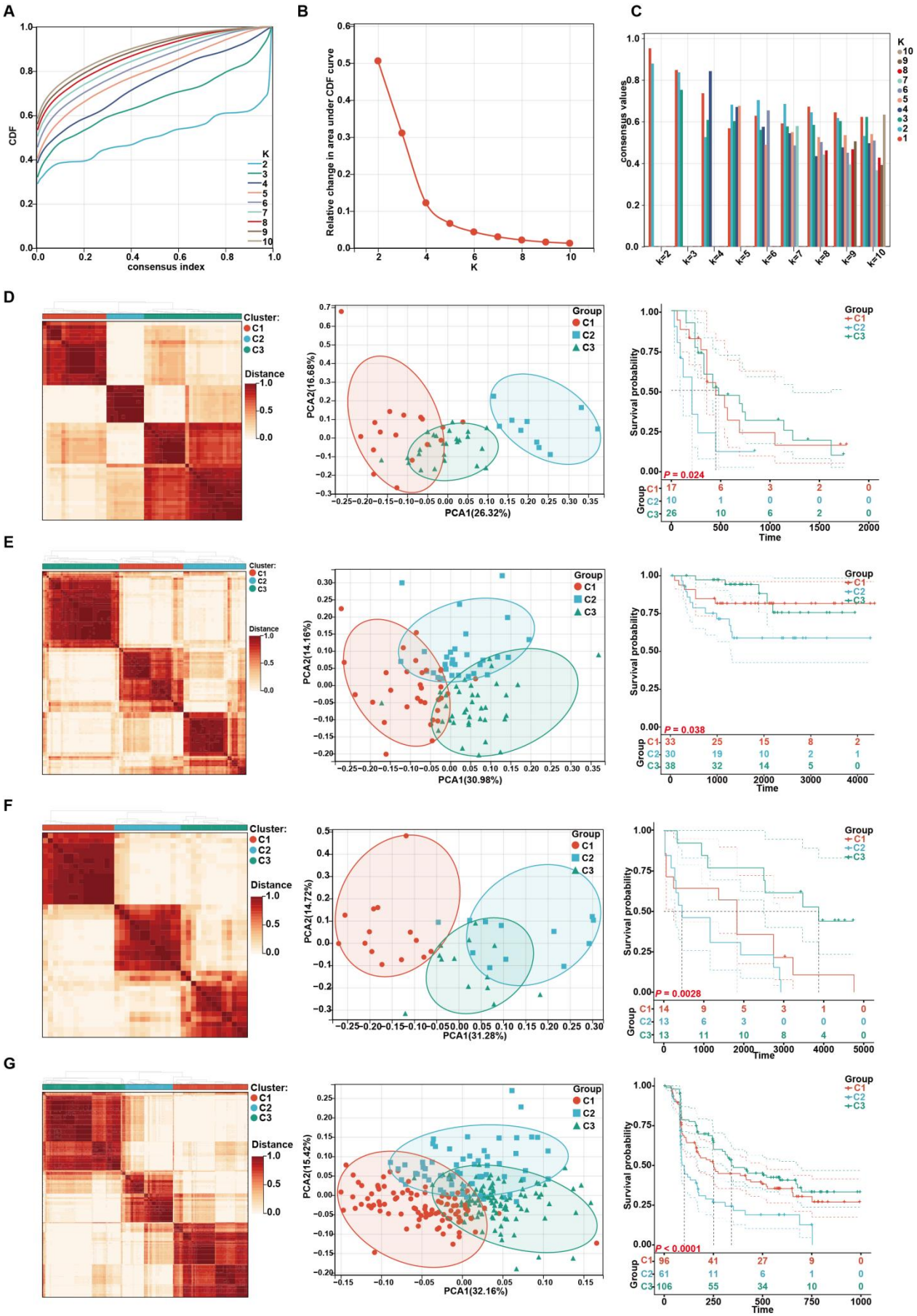
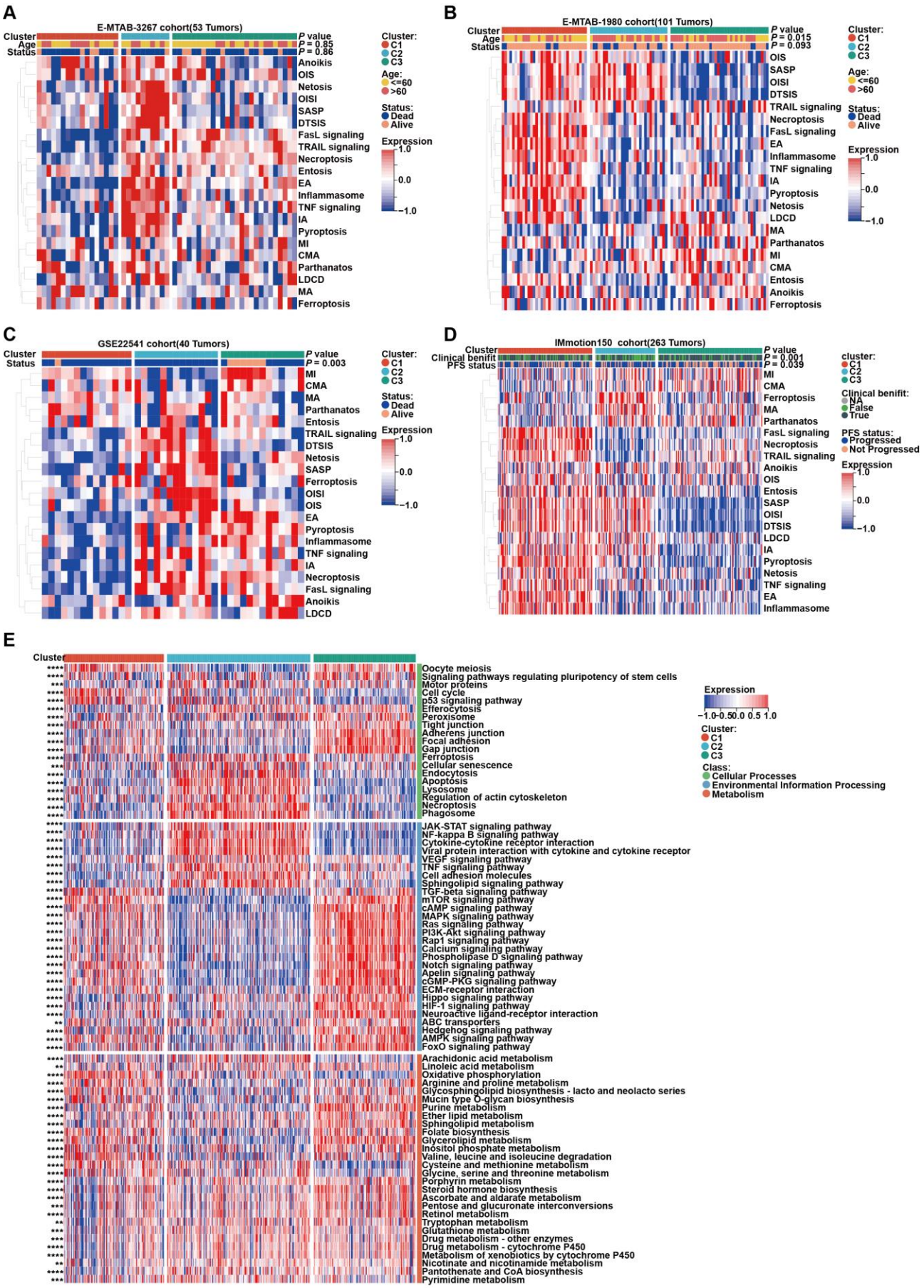

A
CDF
consensus index
K
B
Relative change in area under CDF curve
K
C
consensus values
K
k=2
k=3
k=4
k=5
k=6
k=7
k=8
k=9
k=10
D
Cluster:
C1
C2
C3
Distance
PCA2(16.68%)
PCA1(26.32%)
Group
Survival probability
P = 0.024
Time
E
PCA2(14.16%)
PCA1(30.98%)
P = 0.038
F
PCA2(14.72%)
PCA1(31.28%)
P = 0.0028
G
PCA2(15.42%)
PCA1(32.16%)
P < 0.0001

Fig. S2 Consensus-clustering diagnostics and external three-cluster structures. (A) Cumulative distribution function curves. (B) Relative change in area under the cumulative distribution function. (C) Sample consensus by cluster number in TCGA-KIRC. (D-G) Consensus matrices, principal component analyses, and Kaplan-Meier analyses for E-MTAB-3267, E-MTAB-1980, GSE22541, and IMmotion150; endpoints are PFS for E-MTAB-3267 and IMmotion150, OS for E-MTAB-1980, and DFS for GSE22541.


A
E-MTAB-3267 cohort(53 Tumors)
Cluster
Age
Status
P value
P = 0.85
P = 0.86
Cluster:
C1
C2
C3
Age:
<=60
>60
Status:
Dead
Alive
Expression
1.0
0.0
−1.0
Anoikis
OIS
Netosis
OISI
SASP
DTSIS
FasL signaling
TRAIL signaling
Necroptosis
Entosis
EA
Inflammasome
TNF signaling
IA
Pyroptosis
MI
CMA
Parthanatos
LDCD
MA
Ferroptosis
B
E-MTAB-1980 cohort(101 Tumors)
Cluster
Age
Status
P value
P = 0.015
P = 0.093
Cluster:
C1
C2
C3
Age:
<=60
>60
Status:
Dead
Alive
Expression
1.0
0.0
−1.0
OIS
SASP
OISI
DTSIS
TRAIL signaling
Necroptosis
FasL signaling
EA
Inflammasome
TNF signaling
IA
Pyroptosis
Netosis
LDCD
MA
Parthanatos
MI
CMA
Entosis
Anoikis
Ferroptosis
C
GSE22541 cohort(40 Tumors)
Cluster
Status
P value
P = 0.003
Cluster:
C1
C2
C3
Status:
Dead
Alive
Expression
1.0
0.0
−1.0
MI
CMA
MA
Parthanatos
Entosis
TRAIL signaling
DTSIS
Netosis
SASP
Ferroptosis
OISI
OIS
EA
Pyroptosis
Inflammasome
TNF signaling
IA
Necroptosis
FasL signaling
Anoikis
LDCD
D
IMmotion150 cohort(263 Tumors)
Cluster
Clinical benifit
PFS status
P value
P = 0.001
P = 0.039
cluster:
C1
C2
C3
Clinical benifit:
NA
False
True
PFS status:
Progressed
Not Progressed
Expression
1.0
0.0
−1.0
MI
CMA
Ferroptosis
MA
Parthanatos
FasL signaling
Necroptosis
TRAIL signaling
Anoikis
OIS
Entosis
SASP
OISI
DTSIS
LDCD
IA
Pyroptosis
Netosis
TNF signaling
EA
Inflammasome
E
Cluster
Expression
−1.0 -0.5 0.0 0.5 1.0
Cluster:
C1
C2
C3
Class:
Cellular Processes
Environmental Information Processing
Metabolism
Oocyte meiosis
Signaling pathways regulating pluripotency of stem cells
Motor proteins
Cell cycle
p53 signaling pathway
Efferocytosis
Peroxisome
Tight junction
Adherens junction
Focal adhesion
Gap junction
Ferroptosis
Cellular senescence
Endocytosis
Apoptosis
Lysosome
Regulation of actin cytoskeleton
Necroptosis
Phagosome
JAK-STAT signaling pathway
NF-kappa B signaling pathway
Cytokine-cytokine receptor interaction
Viral protein interaction with cytokine and cytokine receptor
VEGF signaling pathway
TNF signaling pathway
Cell adhesion molecules
Sphingolipid signaling pathway
TGF-beta signaling pathway
mTOR signaling pathway
cAMP signaling pathway
MAPK signaling pathway
Ras signaling pathway
PI3K-Akt signaling pathway
Rap1 signaling pathway
Calcium signaling pathway
Phospholipase D signaling pathway
Notch signaling pathway
Apelin signaling pathway
cGMP-PKG signaling pathway
ECM-receptor interaction
Hippo signaling pathway
HIF-1 signaling pathway
Neuroactive ligand-receptor interaction
ABC transporters
Hedgehog signaling pathway
AMPK signaling pathway
FoxO signaling pathway
Arachidonic acid metabolism
Linoleic acid metabolism
Oxidative phosphorylation
Arginine and proline metabolism
Glycosphingolipid biosynthesis - lacto and neolacto series
Mucin type O-glycan biosynthesis
Purine metabolism
Ether lipid metabolism
Sphingolipid metabolism
Folate biosynthesis
Glycerolipid metabolism
Inositol phosphate metabolism
Valine, leucine and isoleucine degradation
Cysteine and methionine metabolism
Glycine, serine and threonine metabolism
Porphyrin metabolism
Steroid hormone biosynthesis
Ascorbate and aldarate metabolism
Pentose and glucuronate interconversions
Retinol metabolism
Tryptophan metabolism
Glutathione metabolism
Drug metabolism - other enzymes
Drug metabolism - cytochrome P450
Metabolism of xenobiotics by cytochrome P450
Nicotinate and nicotinamide metabolism
Pantothenate and CoA biosynthesis
Pyrimidine metabolism

776

Fig. S3 External CDS profiles and KEGG pathway activity. (A-D) Heatmaps of independently derived CDS clusters in E-MTAB-3267, E-MTAB-1980, GSE22541, and IMmotion150. (E) KEGG GSVA profiles across TCGA-KIRC CDS clusters.

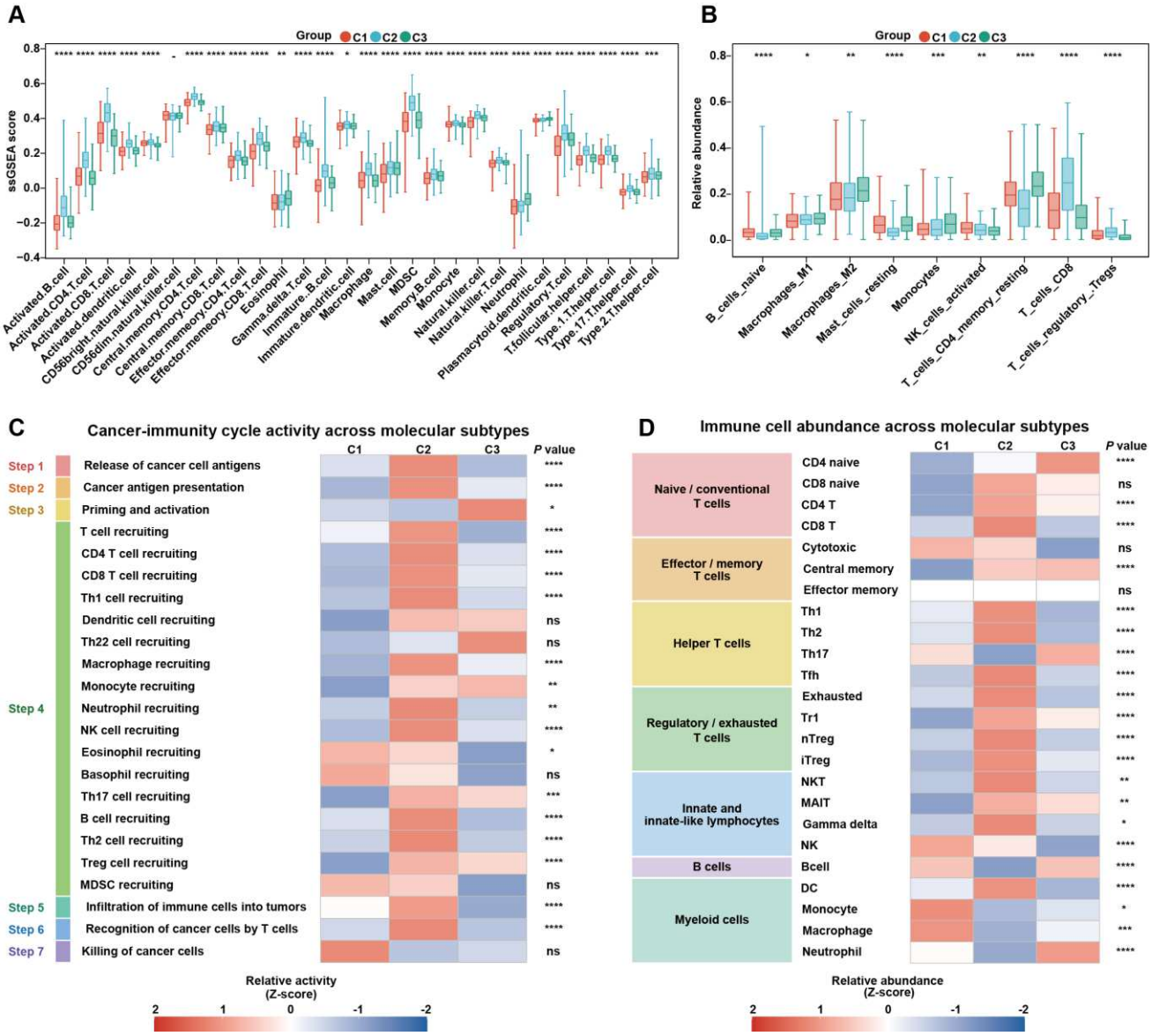


Fig. S4 Immune-cell and cancer-immunity-cycle differences among CDS clusters. (A,B) Immune-cell abundance estimated by ssGSEA and CIBERSORT. (C) Activity of cancer-immunity-cycle steps. (D) ImmuCellAI-inferred immune-cell abundance.

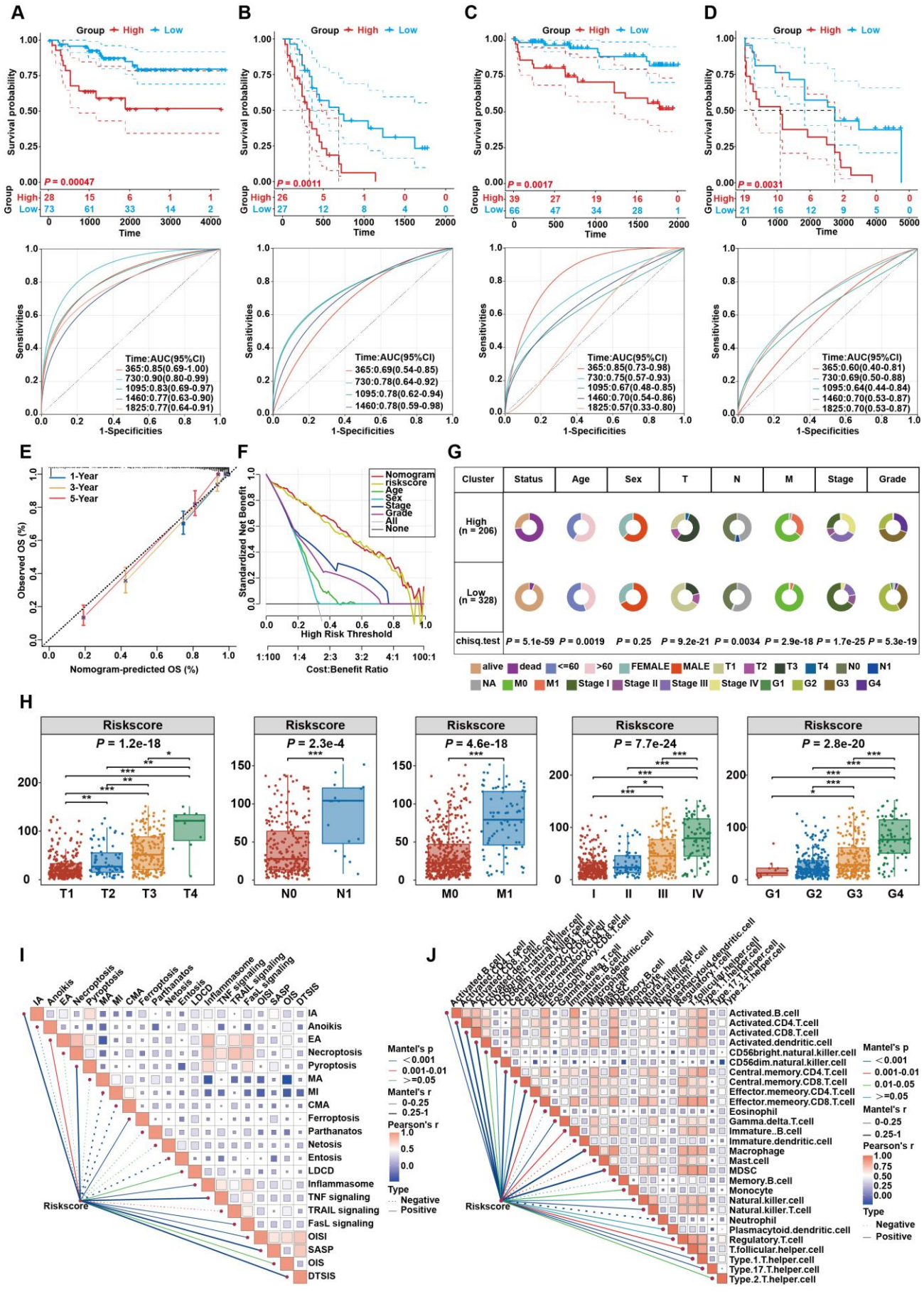
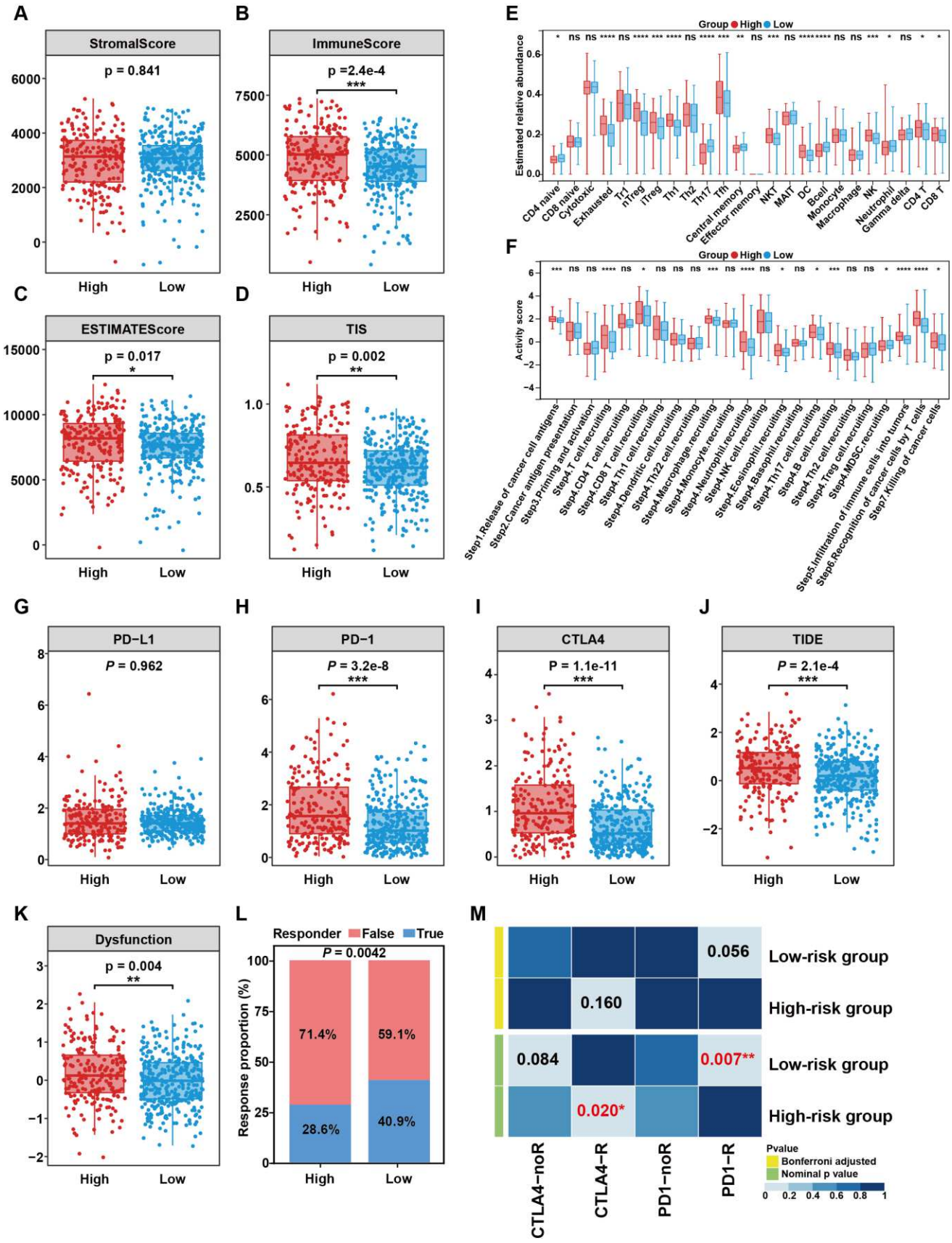

A
B
C
D
Group High Low
Survival probability
P = 0.00047
P = 0.0011
P = 0.0017
P = 0.0031
Time
Sensitivities
1-Specificities
Time:AUC(95%CI)
365:0.85(0.69-1.00)
730:0.90(0.80-0.99)
1095:0.83(0.69-0.97)
1460:0.77(0.63-0.90)
1825:0.77(0.64-0.91)
365:0.69(0.54-0.85)
730:0.78(0.64-0.92)
1095:0.78(0.62-0.94)
1460:0.78(0.59-0.98)
365:0.85(0.73-0.98)
730:0.75(0.57-0.93)
1095:0.67(0.48-0.85)
1460:0.70(0.54-0.86)
1825:0.57(0.33-0.80)
365:0.60(0.40-0.81)
730:0.69(0.50-0.88)
1095:0.64(0.44-0.84)
1460:0.70(0.53-0.87)
1825:0.70(0.53-0.87)
E
1-Year
3-Year
5-Year
Observed OS (%)
Nomogram-predicted OS (%)
F
Nomogram
riskscore
Age
Sex
Stage
Grade
All
None
Standardized Net Benefit
High Risk Threshold
Cost:Benefit Ratio
G
Cluster
Status
Age
Sex
T
N
M
Stage
Grade
High (n = 206)
Low (n = 328)
chisq.test
P = 5.1e-59
P = 0.0019
P = 0.25
P = 9.2e-21
P = 0.0034
P = 2.9e-18
P = 1.7e-25
P = 5.3e-19
alive
dead
<=60
>60
FEMALE
MALE
T1
T2
T3
T4
N0
N1
NA
M0
M1
Stage I
Stage II
Stage III
Stage IV
G1
G2
G3
G4
H
Riskscore
P = 1.2e-18
P = 2.3e-4
P = 4.6e-18
P = 7.7e-24
P = 2.8e-20
T1
T2
T3
T4
N0
N1
M0
M1
I
II
III
IV
G1
G2
G3
G4
I
IA
Anoikis
EA
Necroptosis
Pyroptosis
MA
MI
CMA
Ferroptosis
Parthanatos
Netosis
Entosis
LDCD
Inflammasome
TNF signaling
TRAIL signaling
FasL signaling
OISI
SASP
OIS
DTSIS
Riskscore
Mantel's p
<0.001
0.001-0.01
>=0.05
Mantel's r
0-0.25
0.25-1
Pearson's r
Type
Negative
Positive
J
Activated.B.cell
Activated.CD4.T.cell
Activated.CD8.T.cell
Activated.dendritic.cell
CD56bright.natural.killer.cell
CD56dim.natural.killer.cell
Central.memory.CD4.T.cell
Central.memory.CD8.T.cell
Effector.memeory.CD4.T.cell
Effector.memeory.CD8.T.cell
Eosinophil
Gamma.delta.T.cell
Immature..B.cell
Immature.dendritic.cell
Macrophage
Mast.cell
MDSC
Memory.B.cell
Monocyte
Natural.killer.cell
Natural.killer.T.cell
Neutrophil
Plasmacytoid.dendritic.cell
Regulatory.T.cell
T.follicular.helper.cell
Type.1.T.helper.cell
Type.17.T.helper.cell
Type.2.T.helper.cell

Fig. S5 External evaluation and clinical associations of the prognostic score. (A-D) Kaplan-Meier and time-dependent ROC analyses in E-MTAB-1980, E-MTAB-3267, CPTAC, and GSE22541. (E) Calibration of the 1-, 3-, and 5-year nomogram. (F) Decision curve analysis. (G) Distribution of clinicopathological variables by risk group. (H) Risk-score differences across clinicopathological strata. (I,J) Correlations of risk score with CDS activities and ssGSEA immune-cell signatures. Correlations in panels I and J were calculated using Pearson correlation; endpoints in panels A-D are OS, PFS, OS, and DFS, respectively.


A
StromalScore
p = 0.841
High
Low
B
ImmuneScore
p =2.4e-4
***
C
ESTIMATEScore
p = 0.017
*
D
TIS
p = 0.002
**
E
Group High Low
Estimated relative abundance
CD4 naive
CD8 naive
Cytotoxic
Exhausted
Tr1
nTreg
iTreg
Th1
Th2
Th17
Tfh
Central memory
Effector memory
NKT
MAIT
DC
Bcell
Monocyte
Macrophage
NK
Neutrophil
Gamma delta
CD4 T
CD8 T
F
Group High Low
Activity score
Step1.Release of cancer cell antigens
Step2.Cancer antigen presentation
Step3.Priming and activation
Step4.T cell recruiting
Step4.CD4 T cell recruiting
Step4.CD8 T cell recruiting
Step4.Th1 cell recruiting
Step4.Dendritic cell recruiting
Step4.Th22 cell recruiting
Step4.Macrophage recruiting
Step4.Monocyte recruiting
Step4.Neutrophil recruiting
Step4.NK cell recruiting
Step4.Eosinophil recruiting
Step4.Basophil recruiting
Step4.Th17 cell recruiting
Step4.B cell recruiting
Step4.Th2 cell recruiting
Step4.Treg cell recruiting
Step4.MDSC recruiting
Step5.Infiltration of immune cells into tumors
Step6.Recognition of cancer cells by T cells
Step7.Killing of cancer cells
G
PD−L1
P = 0.962
H
PD−1
P = 3.2e-8
***
I
CTLA4
P = 1.1e-11
***
J
TIDE
P = 2.1e-4
***
K
Dysfunction
p = 0.004
**
L
Responder False True
P = 0.0042
Response proportion (%)
71.4%
59.1%
28.6%
40.9%
M
0.056
Low-risk group
0.160
High-risk group
0.084
0.007**
Low-risk group
0.020*
High-risk group
CTLA4−noR
CTLA4−R
PD1−noR
PD1−R
Pvalue
Bonferroni adjusted
Nominal p value

792

Fig. S6 Immune characteristics of high- and low-risk tumors. (A-D) StromalScore, ImmuneScore, ESTIMATEScore, and T-cell-inflamed signature score. (E) ImmuCellAI-inferred populations. (F) Cancer-immunity-cycle activity. (G-I) CD274, PDCD1, and CTLA4 expression. (J-L) TIDE, dysfunction, and predicted response distributions. (M) SubMap comparison with anti-PD-1 and anti-CTLA-4 response profiles; adjusted results were not statistically significant.

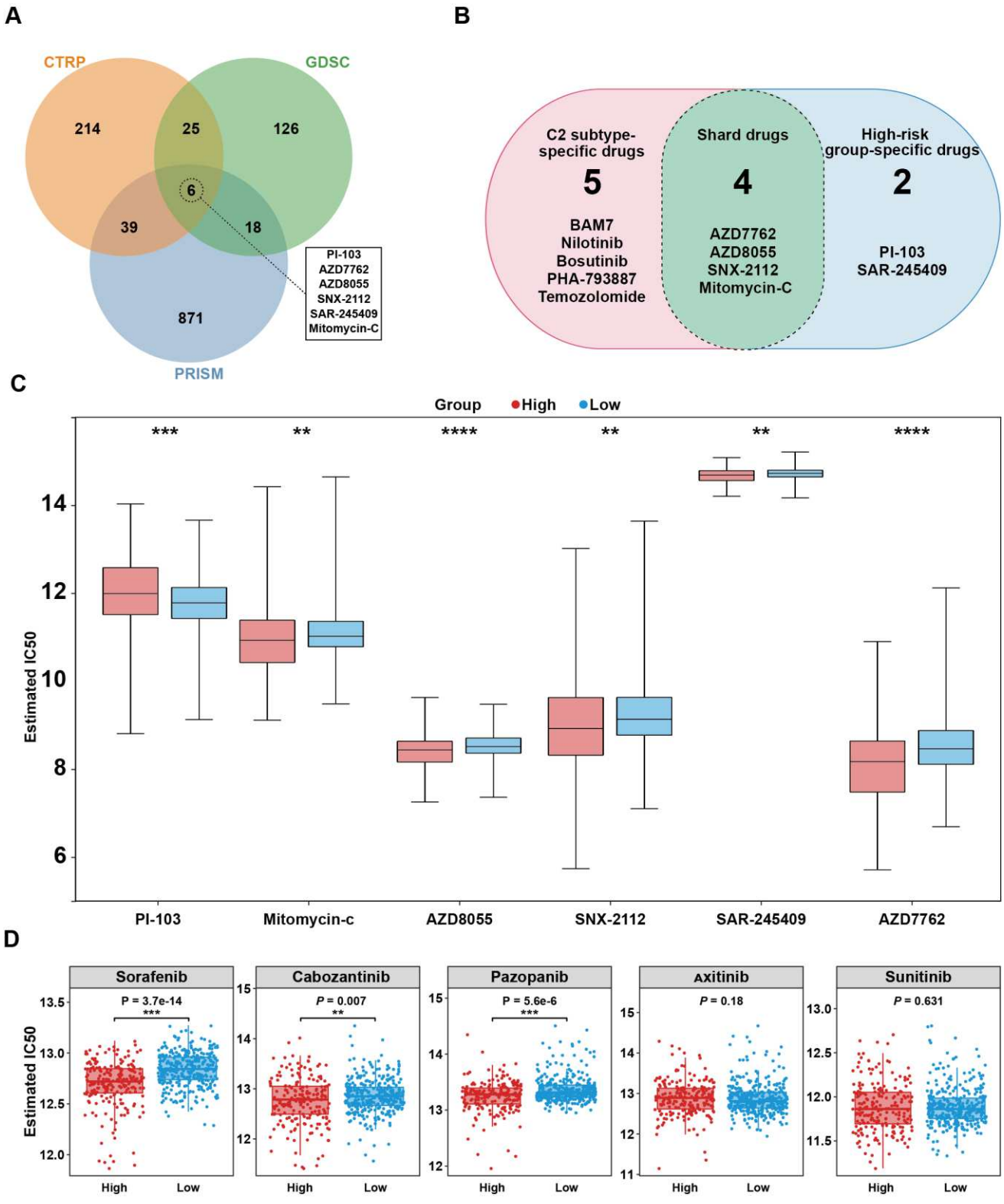
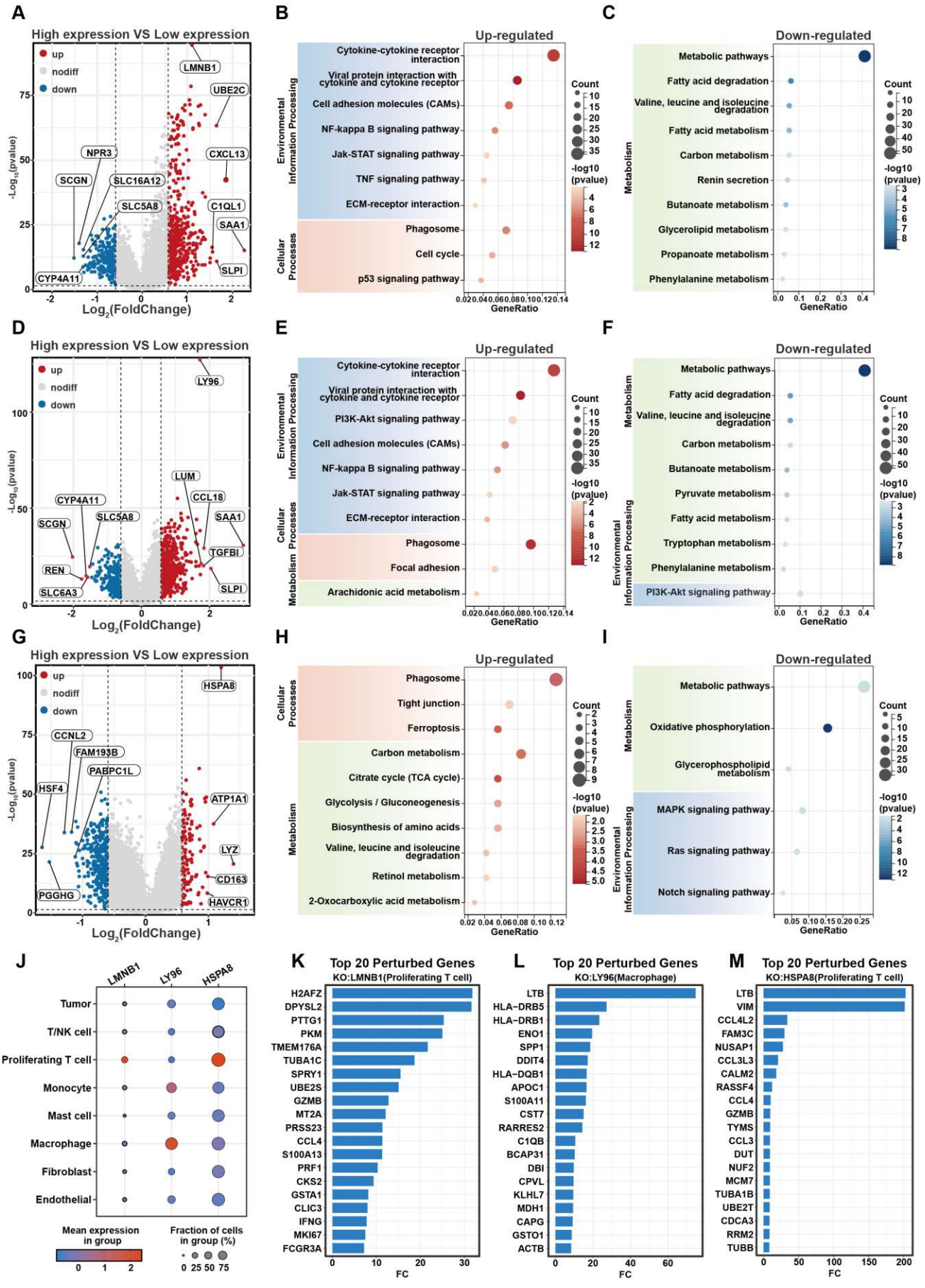


Fig. S7 Risk-associated pharmacogenomic predictions. (A) Candidate drugs shared across three pharmacogenomic resources. (B) Overlap between risk-associated and C2-associated candidates. (C) Predicted response values for six candidate compounds. (D) Predicted response values for five commonly used renal-cancer targeted agents.

802


A
High expression VS Low expression
up
nodiff
down
LMNB1
UBE2C
CXCL13
NPR3
SCGN
SLC16A12
SLC5A8
C1QL1
SAA1
SLPI
CYP4A11
-Log10(pvalue)
Log2(FoldChange)
B
Up-regulated
Cytokine-cytokine receptor interaction
Viral protein interaction with cytokine and cytokine receptor
Cell adhesion molecules (CAMs)
NF-kappa B signaling pathway
Jak-STAT signaling pathway
TNF signaling pathway
ECM-receptor interaction
Phagosome
Cell cycle
p53 signaling pathway
Environmental Information Processing
Cellular Processes
Count
-log10 (pvalue)
GeneRatio
C
Down-regulated
Metabolic pathways
Fatty acid degradation
Valine, leucine and isoleucine degradation
Fatty acid metabolism
Carbon metabolism
Renin secretion
Butanoate metabolism
Glycerolipid metabolism
Propanoate metabolism
Phenylalanine metabolism
Metabolism
D
High expression VS Low expression
LY96
LUM
CCL18
CYP4A11
SLC5A8
SAA1
SCGN
TGFBI
REN
SLC6A3
SLPI
E
Up-regulated
PI3K-Akt signaling pathway
Focal adhesion
Arachidonic acid metabolism
F
Down-regulated
Tryptophan metabolism
Pyruvate metabolism
G
High expression VS Low expression
HSPA8
CCNL2
FAM193B
PABPC1L
HSF4
ATP1A1
LYZ
CD163
PGGHG
HAVCR1
H
Up-regulated
Tight junction
Ferroptosis
Carbon metabolism
Citrate cycle (TCA cycle)
Glycolysis / Gluconeogenesis
Biosynthesis of amino acids
Valine, leucine and isoleucine degradation
Retinol metabolism
2-Oxocarboxylic acid metabolism
I
Down-regulated
Oxidative phosphorylation
Glycerophospholipid metabolism
MAPK signaling pathway
Ras signaling pathway
Notch signaling pathway
J
LMNB1
LY96
HSPA8
Tumor
T/NK cell
Proliferating T cell
Monocyte
Mast cell
Macrophage
Fibroblast
Endothelial
Mean expression in group
Fraction of cells in group (%)
K
Top 20 Perturbed Genes
KO:LMNB1(Proliferating T cell)
H2AFZ
DPYSL2
PTTG1
PKM
TMEM176A
TUBA1C
SPRY1
UBE2S
GZMB
MT2A
PRSS23
CCL4
S100A13
PRF1
CKS2
GSTA1
CLIC3
IFNG
MKI67
FCGR3A
FC
L
Top 20 Perturbed Genes
KO:LY96(Macrophage)
LTB
HLA-DRB5
HLA-DRB1
ENO1
SPP1
DDIT4
HLA-DQB1
APOC1
S100A11
CST7
RARRES2
C1QB
BCAP31
DBI
CPVL
KLHL7
MDH1
CAPG
GSTO1
ACTB
M
Top 20 Perturbed Genes
KO:HSPA8(Proliferating T cell)
LTB
VIM
CCL4L2
FAM3C
NUSAP1
CCL3L3
CALM2
RASSF4
CCL4
GZMB
TYMS
CCL3
DUT
NUF2
MCM7
TUBA1B
UBE2T
CDCA3
RRM2
TUBB

803

Fig. S8 Pathway and single-cell details for prioritized genes. (A-C) LMNB1 high-versus-low DEGs and KEGG enrichment of upregulated and downregulated genes. (D-F) Corresponding analyses for LY96. (G-I) Corresponding analyses for HSPA8. (J) Dot plot of LMNB1, LY96, and HSPA8 expression across annotated single-cell populations. (K-M) Top significantly perturbed genes after virtual knockout of LMNB1 in T cells, LY96 in macrophages, and HSPA8 in T cells.

Online Resource 2 Supplementary tables

Tables S1-S14 are supplied as worksheets in the supplementary workbook.

Table S1. Public datasets, sample availability, clinical endpoints, and treatment annotations.

Table S2. Definitions, sources, and constituent genes of the 21 CDS signatures.

Table S3. TCGA-KIRC CDS-cluster, gene-cluster, risk-group, and survival-status annotations.

Table S4. Cluster-specific differential expression in TCGA-KIRC.

Table S5. Pairwise and omnibus comparisons of Hallmark and KEGG GSVA scores.

Table S6. Drug annotations for nine C2-associated candidate compounds.

Table S7. Expression contrasts for 95 drug-associated genes.

Table S8. Stable differential edges from the C2 versus C1 plus C3 absolute-EPM comparison.

Table S9. Node-level statistics derived from selected stable edges.

Table S10. KEGG enrichment results for 246 prioritized node genes.

Table S11. DEG lists associated with LMNB1, LY96, and HSPA8 expression groups.

Table S12. KEGG enrichment of upregulated and downregulated DEG lists associated with LMNB1.

Table S13. KEGG enrichment of upregulated and downregulated DEG lists associated with LY96.

Table S14. KEGG enrichment of upregulated and downregulated DEG lists associated with HSPA8.

Supplementary Files

This is a list of supplementary files associated with this preprint. Click to download.

- Supplementarytables.xlsx